

# PRECISE DYNAMICAL MASSES OF DIRECTLY IMAGED COMPANIONS FROM RELATIVE ASTROMETRY, RADIAL VELOCITIES, AND HIPPARCOS-GAIA DR2 ACCELERATIONS

TIMOTHY D. BRANDT<sup>1</sup>, TRENT J. DUPUY<sup>2</sup>, AND BRENDAN P. BOWLER<sup>3</sup>

*Draft version February 6, 2019*

## ABSTRACT

We measure dynamical masses for five objects—three ultracool dwarfs, one low-mass star, and one white dwarf—by fitting orbits to a combination of the *Hipparcos-Gaia* Catalog of Accelerations, literature radial velocities, and relative astrometry. Our approach provides precise masses without any assumptions about the primary star, even though the observations typically cover only a small fraction of an orbit. We also perform a uniform re-analysis of the host stars’ ages. Two of our objects, HD 4747B and HR 7672B, already have precise dynamical masses near the stellar/substellar boundary and are used to validate our approach. For Gl 758B, we obtain a mass of  $m = 38.1^{+1.7}_{-1.5} M_{\text{Jup}}$ , the most precise mass measurement of this companion to date. Gl 758B is the coldest brown dwarf with a dynamical mass, and the combination of our low mass and slightly older host-star age resolves its previously noted discrepancy with substellar evolutionary models. HD 68017B, a late-M dwarf, has a mass of  $m = 0.147 \pm 0.003 M_{\odot}$ , consistent with stellar theory and previous empirical estimates based on its absolute magnitude. The progenitor of the white dwarf Gl 86B has been debated in the literature, and our dynamical measurement of  $m = 0.595 \pm 0.010 M_{\odot}$  is consistent with a higher progenitor mass and younger age for this planet-hosting binary system. Overall, these case studies represent only five of the thousands of accelerating systems identified by combining *Hipparcos* and *Gaia*. Our analysis could be repeated for many of them to build a large sample of companions with dynamical masses.

*Subject headings:* methods: statistical, astrometry, celestial mechanics, stars:low-mass, brown dwarfs, white dwarfs

## 1. INTRODUCTION

Dynamical masses represent one of the strongest observational cornerstones of stellar and substellar evolutionary models. They are particularly important for objects that reside off of the main sequence and rapidly evolve in the Hertzsprung-Russell diagram, such as young stars, brown dwarfs, giant planets, and white dwarfs (e.g., Hillenbrand & White 2004; Stassun et al. 2006; Harris et al. 2013; Dupuy & Liu 2017). Combining masses with luminosities and ages (or radii and effective temperatures) offers a powerful way to test and calibrate cooling models of a given composition, providing direct constraints on the internal structure, atmospheric opacity, and radiative evolution of these objects. For young directly imaged substellar companions in particular, dynamical masses can help distinguish among formation mechanisms by breaking degeneracies in hot-, warm-, and cold-start evolutionary models (Marley et al. 2007; Fortney et al. 2008; Spiegel & Burrows 2012; Marleau & Cumming 2014).

A variety of techniques can be used to measure dynamical masses. Most require long-term orbit monitoring of resolved components of a binary system to determine total masses; absolute astrometry or relative radial velocities (RVs) can then constrain the individual component masses (Dupuy et al. 2009a,b; Konopacky et al. 2010; Montet et al. 2015; Bond et al. 2017). Systems in which

the primary star has a measurable radial velocity acceleration are particularly useful. Assuming a known parallax and well-measured astrometric orbit, the primary’s line-of-sight acceleration probes the mass of its companion. These accelerating systems act as “dynamical beacons” and have been used to find and characterize both stellar and substellar companions (e.g., Benedict et al. 2002; Crepp et al. 2015; Cheetham et al. 2018; Bowler et al. 2018). However, the precision of masses for these wide companions is limited by their orbital periods—often decades to centuries—and requires long-baseline monitoring with radial velocities and high-contrast imaging to gradually improve mass constraints.

*Gaia* (Gaia Collaboration et al. 2016) opens up the possibility of measuring the dynamical masses of systems across the sky. *Hipparcos* and *Gaia* measured the motion of stars in an inertial reference frame, the ICRS, defined by distant quasars (Ma et al. 1998; Fey et al. 2015). Differences in the proper motions between *Hipparcos* and *Gaia* imply accelerations in an inertial frame; these may be used to constrain dynamical masses. Calisendorff & Janson (2018) added such a proper motion difference to a study of Gl 758B (Bowler et al. 2018) to refine its dynamical mass, obtaining a final constraint of  $m = 42.4^{+5.6}_{-5.0} M_{\text{Jup}}$ . Previous papers have also explored the use of the *Hipparcos* epoch astrometry in combination with radial velocity or relative astrometry to improve dynamical mass measurements (Han et al. 2001; Sozzetti & Desidera 2010; Sahlmann et al. 2011; Snellen & Brown 2018).

Previous studies have used catalog astrometry at face value, but Brandt (2018) has performed a cross-

<sup>1</sup> Department of Physics, University of California, Santa Barbara, Santa Barbara, CA 93106, USA

<sup>2</sup> Gemini Observatory, Northern Operations Center, 670 N. Aohoku Place, Hilo, HI 96720, USA

<sup>3</sup> Department of Astronomy, The University of Texas at Austin, Austin, TX 78712, USA

calibration of *Hipparcos* and *Gaia* DR2, the *Hipparcos-Gaia* Catalog of Accelerations (HGCA), that accounts for systematics as a function of position on the sky. The HGCA adopts a 60/40 linear combination of the two *Hipparcos* reductions (ESA 1997; van Leeuwen 2007), inflates uncertainties of both *Hipparcos* and *Gaia* DR2, and applies locally variable frame rotations of  $\sim 0.5 \text{ mas yr}^{-1}$  to *Hipparcos* and  $\sim 0.2 \text{ mas yr}^{-1}$  to *Gaia*. All of the resulting astrometry is then placed in the DR2 reference frame. Figure 9 of Brandt (2018) demonstrates the Gaussianity of the residuals between the HGCA’s three proper motion measurements. This Gaussianity makes the catalog well-suited for use in orbit fitting; we employ it here to validate its accuracy and improve on previous dynamical mass estimates.

Combining *Gaia* and *Hipparcos* proper motions provides an acceleration in the plane of the sky. Adding a radial velocity trend gives a full three-dimensional acceleration. Together with a projected separation from direct imaging, this is sufficient to determine a dynamical mass *without observing a substantial fraction of an orbit*. This opens up long-period systems, where the components are well-separated, to dynamical mass measurements. It also reduces the observational effort needed to obtain these masses to intermittent radial velocity monitoring and a few direct imaging snapshots. While this technique can constrain masses to high precision, it does a poorer job of measuring the other orbital parameters. *Gaia* and *Hipparcos* are well-suited to measuring only one parameter, but this parameter is the most physically significant one.

We demonstrate the use of absolute stellar astrometry to constrain masses using a sample of five binaries: Gl 758 (Thalman et al. 2009; Janson et al. 2011), Gl 86 (Els et al. 2001; Lagrange et al. 2006), HR 7672 (Liu et al. 2002), HD 4747 (Crepp et al. 2016, 2018), and HD 68017 (Crepp et al. 2012b). This sample includes one  $\sim 40 M_{\text{Jup}}$  brown dwarf (Gl 758B), two higher-mass brown dwarfs near the stellar/substellar boundary (HR 7672B and HD 4747B), one low-mass M-dwarf (HD 68017B), and one white dwarf (Gl 86B). All of the companions are optically faint, which minimizes their effects on the *Hipparcos* and *Gaia* astrometry. We have not selected this sample systematically, but rather choose five stars with a range of companion properties, well-measured radial velocities, and high signal-to-noise ratio accelerations between the *Hipparcos* and *Gaia* epochs.

The paper is organized as follows. Section 2 contains a uniform re-analysis of the host stars’ ages and basic physical parameters using both activity-age relations and isochrone fitting. Section 3 describes the archival direct imaging and radial velocity measurements that we make use of. Section 4 summarizes the stellar astrometry, derived from *Hipparcos* and *Gaia* DR2 and cross-calibrated by Brandt (2018). Section 5 shows how our approach can provide companion masses to high precision even for short orbital arcs, while Section 6 describes how we actually fit orbits and derive masses. Section 7 discusses our results, and we conclude in Section 8.

## 2. STELLAR AGES AND MASSES

Our targets consist of five field G and K dwarfs, each with a long history of observations including high-resolution spectroscopy. In this section we revisit their fundamental properties of age and mass. The ages, in

particular, are needed to constrain models of their companions. We use both the Bayesian activity age measurement described in Brandt et al. (2014) and a comparison to the PARSEC stellar models (Bressan et al. 2012). One of our stars, the low-metallicity G dwarf HD 68017A, is not fit by these stellar models at any age or mass.

### 2.1. Ages from Stellar Activity and Rotation

Age dating of Sun-like stars by their chromospheric and coronal activity is possible because late-type stars have convective outer envelopes that support magnetic dynamos. As these stars launch a wind, the wind rotates at the same angular velocity as the photosphere out to the Alfvén radius (Mestel 1968). The star imparts its angular momentum to the magnetized wind and spins down (Noyes et al. 1984). This has been recognized as a possible “clock” for many years (Barnes 2003), albeit with large uncertainties, and has been calibrated using clusters and field binaries (e.g. Mamajek & Hillenbrand 2008). The magnetic dynamo also heats the chromosphere and corona, resulting in narrow Ca II HK emission lines and X-ray emission. Both decline as the star spins down, and are much weaker in old field stars than in young clusters (Soderblom 2010, and references therein). At very old ages, gyrochronology may be less useful as an age diagnostic due to a weakening of the stellar dynamo (van Saders et al. 2016). The activity relations have also only been calibrated to activity levels of  $R'_{\text{HK}} \geq -5.0$  corresponding to a Rossby number of 2.2 (Mamajek & Hillenbrand 2008). This is only slightly weaker than the Solar activity level.

Brandt et al. (2014) have developed a Bayesian method using Ca II HK and X-ray emission to constrain the Rossby number and, in turn, the stellar age. This method accounts for uncertainties at old ages by treating all Rossby number measurements above 2.2 as lower limits, resulting in a long tail to old ages for quiescent stars like Gl 758A. It also includes a 5% chance of a star being a catastrophic outlier in the sense that its activity does not reflect its age. We scale a uniform distribution between 0 and 13 Gyr to account for this possibility. We refer to Brandt et al. (2014) for a detailed discussion of the approach.

We collect activity diagnostics from the literature, Ca II *S*-indices from the catalog of Pace (2013) and references therein, and X-ray activities from *ROSAT* (Voges et al. 1999). The Pace catalog has many erroneous values that we have corrected. We adopt the average of the maximum and minimum *S*-indices reported in the literature and transform this to the Mt. Wilson  $R'_{\text{HK}}$ , roughly the log of the ratio of emission in the HK lines to the intensity of the underlying photospheric continuum, using the relations given in Noyes et al. (1984). For stars that are not detected in *ROSAT*, we use nearby detections to estimate the level of X-ray emission that would result in a 5- $\sigma$  detection and use this level as an upper limit.

Table 1 includes our  $R'_{\text{HK}}$  measurements and  $R_X$  values (the log of the ratio of X-ray to bolometric luminosity) for each target. One of our stars, HR 7672A, has multi-decade Mt. Wilson measurements from Baliunas et al. (1995) that we adopt in lieu of an average of literature values. Two of our stars, HD 4747A and HR 7672A, also have rotation periods measured in the literature. These provide a more direct probe of the Rossby number and

TABLE 1  
ADOPTED STELLAR PARAMETERS\*

Star	HIP ID	$\varpi$ (mas)	$\sigma[\varpi]$	$V_T$ (mag)	$\sigma[V_T]^\dagger$	$K_s$ (mag)	$\sigma[K_s]$	$R_X$	$R'_{\text{HK}}$	$P_{\text{rot}}$ (d)	$T_{\text{eff}}$ (K)	[Fe/H]
HD 4747	3850	53.18	0.13	7.226	0.02	5.305	0.029	-5.39	-4.79	27.7	5390	-0.21
Gl 86	10138	92.70	0.05	6.209	0.02	4.125	0.036	-5.42	-4.75	...	5190	-22
HD 68017	40118	46.33	0.06	6.859	0.02	5.090	0.02 <sup>†</sup>	< -5.32	-4.89	...	5531	-0.44
GJ 758	95319	64.06	0.02	6.447	0.02	4.493	0.036	< -5.04	-5.05	...	5426	0.21
HR 7672	98819	56.43	0.07	5.857	0.02	4.388	0.027	-5.88	-4.77 <sup>††</sup>	13.94	5921	0.05

\* References:  $\varpi$  from *Gaia* DR2 (Lindegren et al. 2018),  $V_T$  from *Tycho-2* (Høg et al. 2000),  $K_s$  from 2MASS (Cutri et al. 2003),  $R_X$  from *ROSAT* (Voges et al. 1999),  $R'_{\text{HK}}$  from Pace (2013) and references therein (we have corrected several errors in the catalog),  $T_{\text{eff}}$  and [Fe/H] from Soubiran et al. (2016) and references therein, rotation periods: HR 7672 (Wright et al. 2011); HD 4747 (Peretti et al. 2018).

<sup>†</sup> We have inflated the formal uncertainties to limit the impact of stellar atmospheric modeling and bandpass corrections.

<sup>††</sup> Multi-decade Mt. Wilson measurement (Baliunas et al. 1995)

give smaller errors on the resulting ages (Mamajek & Hillenbrand 2008).

## 2.2. Stellar Model Fitting

We also fit stellar models as an independent measure of the age and stellar mass. We perform the analysis using both a uniform age prior and the age distribution inferred from activity as described in the preceding section. We adopt the PARSEC stellar models (Bressan et al. 2012).

We perform our fits using apparent magnitude, color, distance, and spectroscopic effective temperature and metallicity. We take the measured values from *Tycho* (Høg et al. 2000) and 2MASS (Cutri et al. 2003) as our magnitudes, and transform apparent magnitudes into absolute magnitudes using the parallax measured by *Gaia* DR2 (Gaia Collaboration et al. 2016; Lindegren et al. 2018). We adopt a floor of 0.02 mag on our photometric errors to account for possible systematics in the colors of the stellar models.

For our spectroscopic  $T_{\text{eff}}$  and metallicity, we adopt the median values reported in the literature as tabulated in the PASTEL catalog (Soubiran et al. 2016). While these measurements are all derived from high-resolution, high signal-to-noise spectra, they show significant scatter. We adopt (Gaussian) uncertainties of 75 K in  $T_{\text{eff}}$  and 0.05 in [Fe/H] for all of our stars; this roughly reflects the range of values reported in the literature.

We show results for our stars with three combinations of photometry:  $V_T$  only (sampling the peak of the intensity distribution),  $K_s$  only (sampling the Rayleigh-Jeans tail), and both  $V_T$  and  $K_s$  (providing a photometric  $T_{\text{eff}}$ ). The results are generally consistent, but show significant variation for Gl 758A. One of our G dwarfs, HD 68017A, is incompatible with all of the PARSEC models at high significance.

We perform our analysis on grids of isochrones downloaded from the PARSEC web server<sup>4</sup> on the native *Tycho* and 2MASS photometric systems. We interpolate  $T_{\text{eff}}$  and magnitudes onto a fine grid of masses and use a Salpeter initial mass function,  $dN/dM \propto M^{-2.35}$  (Salpeter 1955), as our mass prior. We then adopt either a uniform prior in age or the prior recovered from the activity-age relation. We calculate our weights as

$$\text{weight} = p[\text{age}] \times \exp[-\chi^2/2], \quad (1)$$

<sup>4</sup> <http://stev.oapd.inaf.it/cgi-bin/cmd>

where  $p[\text{age}]$  is the age prior and

$$\chi^2 = \frac{(V_T - V_{T,\text{obs}})^2}{\sigma_V^2} + \frac{(K_s - K_{s,\text{obs}})^2}{\sigma_K^2} + \frac{(T_{\text{eff}} - T_{\text{eff,obs}})^2}{(75 \text{ K})^2} + \frac{(Z - Z_{\text{obs}})^2}{\sigma_Z^2}. \quad (2)$$

We compute these weights for all models and integrate to obtain marginalized posterior probability distributions.

## 2.3. Results and Notes on Individual Stars

We perform our Bayesian activity-based age dating and our isochrone analysis to all of our stars. Figure 1 shows the activity-based age for HD 68017A. As we discuss in more detail below, no PARSEC model provides an acceptable fit to this star. Figure 2 shows the results of our stellar model fitting for the rest of the sample, with one row of plots for each star. The left column of plots shows the posterior distributions for mass, the middle plots show the posteriors for age, and the right plots show the posteriors for effective temperature. The upper plots for each object assume a uniform prior for age, while the lower plots adopt the posteriors of the activity age analysis (Section 2.1) as their age priors. The thick black lines on the lower age panels show these activity age posteriors.

*HD 4747A*—This early-K/late-G star (Houk & Smith-Moore 1988) has measured X-ray and Ca II HK emission together with a photometric rotation period of just under 28 days (Peretti et al. 2018). These measurements combine to give a relatively precise activity-based age peaked at just under 4 Gyr. The activity-based age is fully consistent with an age based on stellar models, and agrees well with the spectroscopic effective temperature.

*Gl 86A*—The activity-age indicators yield an age of  $\sim 3$ –4 Gyr for this star, in moderate tension with stellar models using both the  $V_T$  and  $K_s$  bands. The star’s kinematics indicate that it is not a member of the thin disk, and suggest an old age (Rocha-Pinto et al. 2002), again in tension with stellar activity. More recently, Fuhrmann et al. (2014) have found that the star has a high ratio of magnesium to iron. This provides a chemical association intermediate between the thin disk and the old, thick disk, corroborating the kinematic evidence. Fuhrmann et al. conjecture that mass transfer from the secondary’s

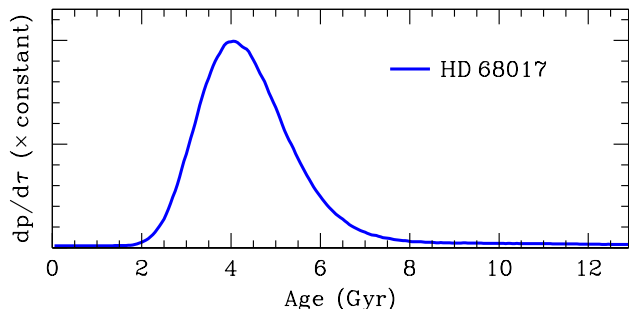


FIG. 1.— Age posterior for the G dwarf HD 68017A using the Bayesian technique of Brandt et al. (2014). Our method uses both X-ray and chromospheric activity indicators to infer a Rossby number and convert this to an age using the calibration of Mamajek & Hillenbrand (2008), adding a uniform distribution weighted by 5% to account for the possibility that the activity age is pathological. To provide a satisfactory fit to HD 68017 with PARSEC stellar models, we would either have to inflate our photometric errors by a factor of  $\sim 10$  or increase its assumed metallicity to  $\sim Z_{\odot}$  and increase its temperature by  $\sim 100$  K.

wind added angular momentum to the primary and accounts for its relatively strong activity.

Farihi et al. (2013) infer a mass of  $0.59 \pm 0.01 M_{\odot}$  for the white dwarf companion. This is based on angular diameter, parallax, and theoretical mass-radius relations (Fontaine et al. 2001). The angular diameter is computed from the white dwarf’s effective temperature, measured by Farihi et al. (2013) both spectroscopically and from broad-band photometry. The *Hipparcos* parallax of  $92.74 \pm 0.32$  mas adopted by Farihi et al. (2013) is consistent with the more precise *Gaia* DR2 parallax of  $92.704 \pm 0.045$  mas. The angular diameter and parallax combine to give a physical radius and a resulting mass of  $0.59 \pm 0.01 M_{\odot}$ . Assuming that a white dwarf of this mass descends from a  $\sim 2 M_{\odot}$  star, this implies a total system age of  $\lesssim 3$  Gyr (Farihi et al. 2013). A very old age for Gl 86 implies a relatively low-mass progenitor for its white dwarf. This conclusion is consistent with the analysis of Lagrange et al. (2006), but is in tension with a remnant mass of  $\sim 0.6 M_{\odot}$ .

*HD 68017A*—This G3 star (Gray et al. 2003) has an upper limit on its X-ray flux but a detection of chromospheric activity slightly above the Solar value. This points to a star very similar to the Sun in both mass and age. However, no PARSEC model at the star’s spectroscopic metallicity of  $-0.44$  can match the observed photometry and *Gaia* parallax. This metallicity is not from a single, isolated analysis: Fuhrmann (2004); Mishenina et al. (2004); Valenti & Fischer (2005); Ramírez et al. (2007); Takeda et al. (2007), and Ramírez et al. (2013) all use high-resolution spectra to infer  $[\text{Fe}/\text{H}]$  values from  $-0.40$  to  $-0.47$ . The best-fitting PARSEC models are at very old ages, but these models are not good fits. We do not show the formal posterior probability distributions from isochrone fitting; the poor goodness-of-fit metric renders these distributions meaningless.

We do not have an explanation for the failure of the stellar models to fit the spectroscopic and photometric constraints at any mass and age. The star’s  $B - V$  color of 0.69 mag (Ducati 2002) is similar to that of the Sun, while its absolute  $V$ -band magnitude of 5.14 mag (com-

puted using the *Gaia* parallax) is slightly less luminous than the Sun. The star does have a close M-dwarf companion, but at visible through near-infrared wavelengths the contrast is  $>100$  (Crepp et al. 2012b). The flux added by the companion is smaller than the photometric errors, and should also have a negligible effect on stellar parameters inferred from optical spectroscopy. In the absence of a constraint from stellar models, Figure 1 shows the age inferred from stellar activity alone.

*Gl 758A*— Our analysis of Gl 758A favors an old age,  $\gtrsim 6$  Gyr, based largely on its low levels of chromospheric and coronal activity. These are in mild tension with the PARSEC isochrone ages. Vigan et al. (2016) used Gl 758A’s  $V$ -band magnitude, spectroscopic metallicity, and effective temperature to derive an age of  $2.2 \pm 1.4$  Gyr based on the same PARSEC models that we use. This analysis corresponds to the blue solid curve in Figure 2, with a lower limit of 600 Myr based on a non-detection of lithium (Janson et al. 2011; Vigan et al. 2016).

When only using  $V_T$  and adopting a uniform age prior, our modeling using the PARSEC isochrones favor a younger age and a higher mass. This is also true, though slightly less so, when using only  $K_s$ . In both cases the age posteriors are consistent with the age inferred from activity; they do not exclude an old age. Using both  $V_T$  and  $K_s$  gives a photometric constraint on effective temperature. The right panel of Figure 2 shows that these photometric  $T_{\text{eff}}$ , which are implicit in the models, are in mild tension with the spectroscopic effective temperature. However, the large, homogeneous, and calibrated analysis of Brewer et al. (2016) produces a very low  $T_{\text{eff}}$  of 5358 K even as those authors note strong systematic uncertainties in spectroscopic determinations of  $T_{\text{eff}}$  and their adoption of an empirical offset. Adopting the Brewer et al. (2016) value would push the tension with the photometric  $T_{\text{eff}}$  in the other direction. Because of the risks in relying on a precise value of  $T_{\text{eff}}$ , we favor a relatively broad prior on  $T_{\text{eff}}$  and the use of an independently calibrated activity age prior.

Regardless of which photometric band(s) we adopt, including the activity age as our prior conclusively favors an old age for the system. These older ages of  $\sim 6$ – $10$  Gyr give a stellar mass between  $0.89$  and  $0.97 M_{\odot}$  at 90% confidence (the exact range depends on the choice of photometric bands). An old age also eases the tension between the observed luminosity of Gl 758B and models of substellar evolution (Bowler et al. 2018). Finally, we note that other authors have derived masses and ages for Gl 758A from different stellar evolutionary models. Brewer et al. (2016), for example, obtain a mass of  $0.92 \pm 0.03 M_{\odot}$  and an age of 4.6 to 10.4 Gyr by combining the Yonsei-Yale models (Demarque et al. 2004; Spada et al. 2013) with their spectroscopic measurements. These age constraints, which were derived using a lower value of  $T_{\text{eff}}$ , agree well with our activity age.

*HR 7672A*—This G0 star (Gray et al. 2006) has Ca II HK emission measured from multi-decade Mt. Wilson data (Baliunas et al. 1995) and a photometric rotation period (Wright et al. 2011). This provides the best activity-based age of any star in our sample, centered at 2 Gyr.

HR 7672A also has an angular diameter of  $0.584 \pm$

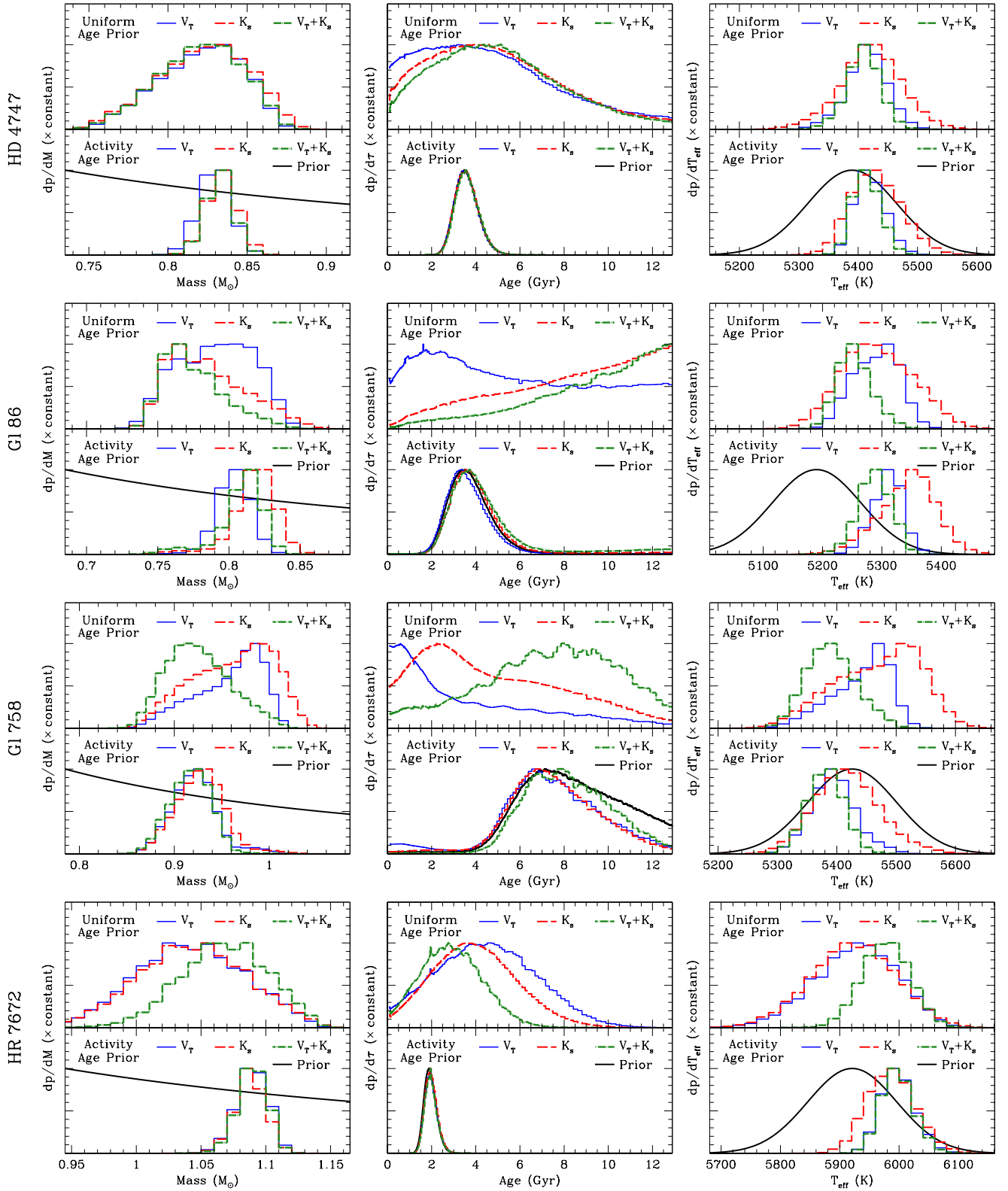


FIG. 2.— Mass, age, and  $T_{\text{eff}}$  posterior probability distributions for our G and K dwarfs computed using the PARSEC isochrones (Bressan et al. 2012) with a Salpeter mass prior and either a uniform age prior or one derived from stellar activity according to the method described in Brandt et al. (2014). We do not show HD 68017, which the PARSEC models are unable to fit. Our adopted stellar parameters are given in Table 1. The isochrone ages are in good agreement with the activity ages for all of these stars. Gl 758 has posteriors that differ significantly depending on which photometric band(s) we use; this likely reflects a mismatch between our spectroscopic  $T_{\text{eff}}$  and the photometric  $T_{\text{eff}}$  (as measured across the  $V_T$  and  $K_s$  wavelength baseline) implicit in the PARSEC isochrones.

0.010 mas measured interferometrically (Crepp et al. 2012b), or a radius of  $1.113 \pm 0.019 R_{\odot}$  adopting the *Gaia* DR2 parallax. Crepp et al. (2012a) used this radius to obtain an isochrone-based age of  $2.5 \pm 1.8$  Gyr. The activity-based age is consistent with the isochrone-based ages, but is much more precise. It favors a slightly higher effective temperature than the spectroscopic value, though well within our adopted uncertainty.

### 3. RADIAL VELOCITY AND DIRECT IMAGING ASTROMETRY

All of our targets have both direct imaging and radial velocity data available in the literature. In this section, we provide a brief summary of the observations for each star. The radial velocity time series are mostly taken with the HIRES instrument on Keck (Vogt et al. 1994), as published by Butler et al. (2017). Gl 86 is a southern target with a radial velocity time series from the UCLES échelle spectrograph (Diego et al. 1990) on the Anglo-Australian Telescope. Its data were published in Butler et al. (2006). The direct imaging astrometry comes from a variety of sources; they are listed in Table 2.

#### 3.1. HD 4747

The radial velocity curve for HD 4747A is from HIRES, as published by Butler et al. (2017). As for our other targets with HIRES data, the spectra were reduced and calibrated using the same techniques as the California Planet Survey (Howard et al. 2010). The radial velocity time series for HD 4747A runs from 1996 through 2013, covering nearly 17 years with 49 measurements. The median uncertainty of the radial velocities is  $1.65 \text{ m s}^{-1}$ , and the radial velocity curve contains a significant amount of orbital information beyond a simple linear trend.

Direct imaging observations of HD 4747 include four different instruments spanning nearly ten years. High-contrast imaging was obtained in 2008 using NACO (Lenzen et al. 2003; Rousset et al. 2003) on VLT. Initially a non-detection, the data were re-reduced by Peretti et al. (2018). These authors constructed  $\chi^2$  maps at different roll angles to obtain astrometric uncertainties, and added a small additional amount of error in quadrature. More recently, the system has been observed by NIRC2 on Keck (Crepp et al. 2016), by GPI (Crepp et al. 2018), and by SPHERE (Peretti et al. 2018). The NIRC2 observations in 2014 and 2015 were taken as part of the TRENDS survey, and were reduced and presented in (Crepp et al. 2016). The more recent SPHERE observations have the lowest claimed uncertainties, particularly in separation, where the fractional error is 1%.

The two GPI position angle measurements by Crepp et al. (2018) are  $\sim 2\sigma$  discrepant with one another. The first of the two GPI measurements also has a position angle  $\sim 4\sigma$  discrepant from the trend favored by the rest of the astrometry. We therefore omit these measurements from our fit, adopting the same astrometry as Peretti et al. (2018). Bowler et al. (2018) encountered similar difficulties in combining astrometry of Gl 758B from different instruments; those authors finally restricted their analysis to NIRC2.

The combination of ten years of companion astrometry, twenty years of radial velocities, and a model isochrone-derived host-star mass of  $0.856 \pm 0.014 M_{\odot}$  enabled Peretti et al. (2018) to derive a companion mass of

$m = 70.2 \pm 1.6 M_{\text{Jup}}$ . This is somewhat higher than the companion mass of  $m = 65.3_{-3.3}^{+4.4} M_{\text{Jup}}$  derived by Crepp et al. (2018) using a host star mass of  $0.82 \pm 0.04 M_{\odot}$ .

#### 3.2. Gl 86

Gl 86 is a southern target ( $\delta \approx -51^\circ$ ) and is not accessible from Keck. The radial velocity time series for this object was taken with the UCLES échelle spectrograph (Diego et al. 1990) on the Anglo-Australian Telescope. Butler et al. (2006) published 42 radial velocity measurements taken between 1998 and 2005 with a median uncertainty of  $4.2 \text{ m s}^{-1}$ . The radial velocities show both a strong linear trend and a periodic signal from an inner companion (Gl 86 b) on a 15.8 day orbit (Queloz et al. 2000). Han et al. (2001) used the *Hipparcos* epoch astrometry together with the radial velocity amplitude to obtain a mass of  $m_b \sim 15 M_{\text{Jup}}$ . However, Pourbaix & Arenou (2001) showed that the *Hipparcos* precision is insufficient to establish the true mass of the inner planet. A full astrometric analysis may be possible once the *Gaia* epoch astrometry is published.

Relative astrometry for the companion extends over more than a decade, beginning with the first detection by Els et al. (2001) using ADONIS-SHARPII (Beuzit et al. 1997). Those authors detected the companion at three observational epochs in late 2000, but their formal astrometric errors render the astrometric measurements inconsistent with one another. Their tabulated astrometric errors also do not account for the  $\sim 25$  mas uncertainty they quote for the position of the bright Gl 86A. In the text, Els et al. give a separation of  $1''.73 \pm 0''.03$  and a position angle of  $119^\circ \pm 1^\circ$ . We adopt these values at 2000.82, the mean of their three observational epochs.

Lagrange et al. (2006) used VLT/NACO to obtain additional astrometric measurements from 2003 to 2005 and also performed an orbital fit, finding the companion to be a  $\sim 0.5 M_{\odot}$  white dwarf. Mugrauer & Neuhäuser (2005) obtained another astrometric measurement in January of 2005, also with VLT/NACO, and independently confirmed the white dwarf identity of the companion. The Mugrauer & Neuhäuser data were taken with NACO in spectral differential imaging (SDI) mode. They used a *Hipparcos* binary to calibrate the plate scale.

The Lagrange et al. measurements were taken using both the wide-field camera S27 and the narrow-field camera S13. In the case of the 2004 observation using S13, the quoted uncertainty in separation,  $0''.014$ , is no larger than that implied by the quoted uncertainty in the plate scale ( $13.25 \pm 0.10 \text{ mas pixel}^{-1}$ ) at Gl 86B's separation. Astrometric calibration for all images, both those taken with S13 and S27, was done using the  $\Theta_1$  Ori C system. However, the S27 camera in particular has nonlinear distortion averaging a few tenths of a pixel, or  $\sim 5$  mas, and this distortion varies strongly across the field-of-view (Plewa et al. 2015). In many places, even near the center of the field-of-view, it is  $\gtrsim 10$  mas. Though the distortion correction varies with time (Plewa et al. 2015), it may be possible to improve the astrometry with a re-reduction of these archival data. For our analysis here, we add 10 mas of astrometric uncertainty in quadrature with the published values of Lagrange et al. (2006). There does not appear to be a published distortion correction for the SDI camera on NACO; in the absence of one, we add

the same 10 mas in uncertainty to these measurements. Mugrauer & Neuhäuser (2005) only provided one significant figure for their separation. As a result, we round our separation uncertainty up to 20 mas.

The four VLT/NACO data points that we use derive from three separate cameras. Field distortion could have induced similar errors to more than one data point (depending on the location and orientation of the calibration field and science imaging), potentially introducing covariance between astrometric measurements.

Farihi et al. (2013) obtained precise *HST* astrometry in 2012, giving an 11 year baseline between the earliest and latest astrometry. Even after our error inflation, the four VLT/NACO points from 2003-5 are only marginally consistent with the slope of the separation vs. time relation of  $57 \text{ mas yr}^{-1}$  implied by the earliest and latest astrometry ( $\chi^2 = 5.1$  for three degrees of freedom). This suggests that our uncertainties for the NACO data might remain underestimated. One additional piece of circumstantial evidence for underestimated errors in NACO astrometry comes from Peretti et al. (2018). Those authors re-reduced VLT/NACO imaging taken in SDI mode for HD 4747B and derived a separation uncertainty of 11 mas. However, this point remained nearly  $2\sigma$  discrepant with their orbital fit.

### 3.3. HD 68017

HD 68017A is a G dwarf with an M dwarf companion indicated by a nonlinear radial velocity trend and later discovered by direct imaging (Crepp et al. 2012b). We use the radial velocity time series obtained with HIRES on Keck and published by Butler et al. (2017). These measurements extend from 1997 to 2014, comprising 182 radial velocities with a median precision of  $2.6 \text{ ms}^{-1}$ . (We exclude one highly discrepant radial velocity measurement with very low counts from 2454547.8 JD.) The RVs show a strong trend with substantial curvature. Crepp et al. (2012b) reported a photometric mass estimate of  $0.15 \pm 0.01 M_{\odot}$  based on the empirical mass-luminosity relation of Delfosse et al. (2000), consistent with the lower limit of  $>0.08 M_{\odot}$  implied by the radial velocity amplitude.

There are only two relative astrometry epochs available for HD 68017, both from 2011–2012, and taken using NIRC2 on Keck (Crepp et al. 2012b). The companion is relatively bright in the *H* band, giving very small astrometric errors, though Crepp et al. (2012b) did not perform a full orbital analysis. Perhaps due to the stellar nature of the companion it has not been targeted for subsequent astrometric follow-up.

Bowler et al. (2018), also using NIRC2, added 1 mas to the positional errors of both Gl 758A and its companion to account for uncertainties in the distortion correction. We repeat that procedure here, adding in quadrature 1.4 mas to the separations and  $0.14$  to the PAs reported by Crepp et al. (2012b), with Table 2 giving the errors as used in our analysis. Bowler et al. (2018) added another 4.3 mas in quadrature to the separation uncertainties for Gl 758B to achieve an acceptable reduced  $\chi^2$  in their orbital fit. We do not repeat that step here, though further error inflation may be warranted as the data were collected with the same instrument (NIRC2) as for Gl 758B.

### 3.4. Gl 758

All of our data for Gl 758, apart from the *Gaia* and *Hipparcos* astrometry, were published in Bowler et al. (2018). Following that paper, we combine the HIRES radial velocity time series for Gl 758A (Butler et al. 2017) with data from the McDonald observatory and the Automated Planet Finder at Lick Observatory. The McDonald measurements used the Tull échelle spectrograph (Tull et al. 1995) as part of a radial velocity planet search (Cochran et al. 1997; Endl et al. 2016); the data for Gl 758A span 19 years with a typical uncertainty of  $4.6 \text{ ms}^{-1}$ . Since 2013, Gl 758A has been observed with the Automated Planet Finder at Lick Observatory (APF, Vogt et al. 2014) as part of a search for rocky planets (Fulton et al. 2015). This program collected 250 spectra with a typical uncertainty of  $1.4 \text{ ms}^{-1}$ . The Keck HIRES time series encompasses 262 spectra with a median uncertainty of  $1.2 \text{ ms}^{-1}$ .

The relative astrometry used by Bowler et al. (2018) is exclusively from the NIRC2 camera on the Keck telescope with natural guide star adaptive optics (Wizinowich et al. 2000). These observations comprise four epochs spanning 7.4 years, from May 2010 through October 2017. Bowler et al. (2018) processed the data using the locally optimized combination of images algorithm (LOCI, Lafrenière et al. 2007) for data taken in angular differential imaging mode (ADI, Marois et al. 2006). The data processing pipeline is described in Bowler et al. (2015); the distortion corrections were derived by Yelda et al. (2010) for pre-2015 data and by Service et al. (2016) for subsequent data, after a pupil realignment. Detections of two background objects in the field were used to validate the astrometry. The calibrated Keck/NIRC2 high-contrast imaging gives relative positions of Gl 758A and Gl 758B to an accuracy of 5 mas and marginally detect curvature in the orbit.

### 3.5. HR 7672

HR 7672A was first monitored as part of the Lick planet search in 1987 (Cumming et al. 1999). Since 1994, it has also been monitored by HIRES on Keck (Butler et al. 2017). HR 7672A displayed a strong linear trend in its radial velocities; the brown dwarf responsible for this trend was first imaged in 2001 (Liu et al. 2002). The published HIRES radial velocity time series now extends to 2014, a total baseline of twenty years (Butler et al. 2017). It comprises 188 measurements with a median uncertainty of  $1.45 \text{ ms}^{-1}$ . Lick spectroscopy adds another 80 measurements with a reported median uncertainty of  $1.0 \text{ ms}^{-1}$ , extending the temporal coverage to nearly thirty years. Curvature is clearly visible in the full time series, which now covers a substantial fraction of the orbit.

HR 7672B has a long history of being imaged with corresponding relative astrometry. Liu et al. (2002) obtained the first measurement in 2001 using the Hokupa'a adaptive optics system on Gemini-North (Graves et al. 1998); they also obtained two astrometric measurements using natural guide star adaptive optics on Keck (Wizinowich et al. 2000). Liu et al. (2002) obtained a dynamical lower limit on the mass of  $48 M_{\text{Jup}}$ . In 2002, Boccaletti et al. (2003) obtained astrometry and photometry using the PALAO adaptive optics system on Palomar

TABLE 2  
SUMMARY OF DIRECT IMAGING ASTROMETRY

Date	$\rho$ (arcsec)	$\sigma_\rho$	PA (degrees)	$\sigma_{PA}$	Ref
HD 4747					
2008.69	0.608	0.011	156.4	1.3	P18
2014.78	0.6065	0.0070	180.04	0.62	C16
2015.02	0.6066	0.0064	180.52	0.58	C16
2015.73	0.604	0.007	184.9	0.9	C16
2015.98	0.585	0.014	185.2	0.3	C18
2015.98	0.583	0.014	184.4	0.3	C18
2016.95	0.5944	0.0051	187.2	0.3	P18
2016.95	0.5950	0.0051	187.6	0.3	P18
2017.74	0.5812	0.0058	190.6	0.5	P18
2017.74	0.5808	0.0063	190.6	0.7	P18
Gl 86					
2000.82	1.73	0.03	119	1	E01
2003.87	1.906	0.015	107.5	0.5	L06
2004.73	1.941	0.017	105.3	0.6	L06
2005.03	1.93	0.02	104.0	0.4	M05
2005.57	1.969	0.015	102.7	0.5	L06
2012.25	2.351	0.002	88.96	0.04	F13
HD 68017					
2011.15	0.5945	0.0015	248.20	0.17	C12b
2012.02	0.5746	0.0015	240.30	0.17	C12b
Gl 758					
2010.33	1.848	0.005	200.6	0.3	B18
2013.50	1.743	0.005	205.7	0.2	B18
2016.49	1.626	0.005	210.3	0.4	B18
2017.77	1.588	0.005	213.5	0.3	B18
HR 7672					
2001.64	0.786	0.006	157.9	0.5	L02
2001.94	0.794	0.005	157.3	0.6	L02
2002.54	0.788	0.006	156.6	0.9	B03
2006.69	0.750	0.080	155.0	5.0	S09
2007.73	0.742	0.035	151.8	2.9	C12a
2011.37	0.519	0.006	147.1	0.5	C12a

\* References abbreviated as: B03 (Boccaletti et al. 2003); B18 (Bowler et al. 2018); C12a (Crepp et al. 2012a); C12b (Crepp et al. 2012b); C16 (Crepp et al. 2016); C18 (Crepp et al. 2018); E01 (Els et al. 2001); F13 (Farihi et al. 2013); L06 (Lagrange et al. 2006); L02 (Liu et al. 2002); M05 (Mugrauer & Neuhäuser 2005); P18 (Peretti et al. 2018); S09 (Serabyn et al. 2009).

(Troy et al. 2000); they obtained a mass of 58–72  $M_{Jup}$  from models of substellar evolution.

In 2007, Serabyn et al. (2009) detected the brown dwarf using a small, well-corrected aperture on the Palomar-Hale telescope. The small aperture leads to large astrometric uncertainties. While we do include the measurement, the error bars are large enough that it does not significantly inform our fit. Most recently, Crepp et al. (2012a) obtained precise astrometry using NIRC2 on Keck. Those authors also reduced NACO observations from 2007. The NACO images, like the Palomar-Hale measurements, are too noisy to be of much value in our orbit fitting.

Crepp et al. (2012a) performed an orbit fit using both radial velocities and companion astrometry, and they obtained a mass of  $m = 68.7_{-3.1}^{+2.4} M_{Jup}$  using a model-derived host star mass of  $M = 1.08 \pm 0.04 M_\odot$ .

#### 4. HOST-STAR ASTROMETRY

This paper adds absolute astrometric measurements of the host stars to existing radial velocity data and direct imaging astrometry. The host-star absolute astrometry comes from a combination of *Hipparcos* and *Gaia*, two satellite missions with a  $\sim 25$ -year time baseline between them. To measure acceleration we use the deviations between three proper motion measurements:

- The *Hipparcos* proper motions near epoch 1991.25;
- The *Gaia* DR2 proper motions near epoch 2015.5; and
- The *Gaia* – *Hipparcos* positional difference divided by the  $\sim 25$  year time baseline (hereinafter referred to as the scaled positional difference).

The long baseline between the missions makes them sensitive to companions with periods as long as centuries. It also renders the scaled positional difference our most precise proper motion measurement. The differences between these proper motion measurements probe the acceleration of the star in an inertial reference frame.

Brandt (2018) has performed a cross-calibration of *Hipparcos* and *Gaia*, placing all three proper motion measurements in the reference frame defined by *Gaia* DR2 (Gaia Collaboration et al. 2018; Lindegren et al. 2018). This reference frame is a close approximation of the International Celestial Reference System (ICRS, Ma et al. 1998; Fey et al. 2015). Figure 1 of Brandt (2018) confirms that such a calibration is necessary: the proper motions taken directly from the catalogs are inconsistent with the standard assumptions of Gaussianity. There are several components to the final cross-calibration:

- Weights for a linear combination of the two *Hipparcos* reductions (ESA 1997; van Leeuwen 2007);
- Propagation of positions to their central epochs in each catalog;
- Local offsets between the reference frames defined by the *Hipparcos* proper motions, the *Gaia* DR2 proper motions, and the scaled positional differences;
- A global error inflation term for *Hipparcos*, to be added diagonally to the published covariance matrices; and
- A local error inflation factor for the *Gaia* DR2 covariance matrices (averaging  $\sim 1.7$  for the errors, or  $\sim 1.7^2$  for the covariances).

The Brandt (2018) catalog provides the three proper motions all in the reference frame of *Gaia* DR2. Figure 9 of that paper demonstrates that the distribution of residuals do follow the assumed Gaussian distributions after applying these cross-calibrations. Close binaries in which one star makes a non-negligible contribution to the flux can still be problematic. Also, Figure 9 of Brandt (2018) shows that the lowest-precision stars in *Gaia* have non-Gaussian tails in their proper motion residuals.

For the stars presented in this paper, the scaled difference in right ascension and declination between *Hipparcos* or *Gaia* is easily the most precise proper motion



measurement ( $\mu_{HG}$ ). We therefore adopt the differences between this and the *Hipparcos* or *Gaia* proper motion as our astrometric constraints on the host-star orbit, computing two differences from our three proper motions. We define them here as, e.g.,

$$\Delta\mu_{\alpha^*,Hip} = \mu_{\alpha^*,Hip} - \mu_{\alpha^*,HG}, \quad (3)$$

where  $\mu_{\alpha^*,Hip}$  is the *Hipparcos* proper motion with the  $\cos\delta$  factor included, and  $\mu_{\alpha^*,HG}$  is the position difference between *Hipparcos* and *Gaia* DR2 divided by the time baselines between the measurements.

The *Hipparcos* and *Gaia* proper motions are almost entirely independent, apart from a tiny covariance arising from the use of *Gaia* parallaxes to improve the other *Hipparcos* astrometry (Brandt 2018). For this reason, and because the scaled positional difference is so precise, we may neglect the (tiny) covariance between  $\Delta\mu_{\alpha^*,Hip}$  and  $\Delta\mu_{\alpha^*,Gaia}$ . If this covariance were significant, we would have to treat the three proper motions separately and solve for the proper motion of the system's center of mass.

Table 3 lists the two proper motion differences and their associated covariance matrices, as computed from the Brandt (2018) catalog.

## 5. SINGLE EPOCH COMPANION MASSES

The combination of *Hipparcos*, *Gaia* DR2, direct imaging astrometry, and radial velocity monitoring makes it possible to determine companion masses to high precision even for very long period systems, and without needing any external information about the host star's mass. Together, these measurements give the projected separation of the companion relative to the host star  $\rho$ , the host star's astrometric acceleration  $a_{\alpha\delta}$ , and the host star's acceleration along the line-of-sight  $a_{RV}$  (as measured using radial velocity). These two accelerations are in the inertial frame defined by the system's center of mass. Together,  $\rho$ ,  $a_{\alpha\delta}$  and  $a_{RV}$  uniquely determine the companion mass via the equations

$$a_{\alpha\delta} = \frac{GM_B}{r_{AB}^2} \cos\phi, \quad (4)$$

$$a_{RV} = \frac{GM_B}{r_{AB}^2} \sin\phi, \quad \text{and} \quad (5)$$

$$\rho = r_{AB} \varpi \cos\phi, \quad (6)$$

where  $\phi$  is the angle between the position vector separating the two bodies and the plane of the sky,  $r_{AB}$  is the absolute separation of the two bodies,  $\varpi$  is the parallax,  $M_B$  is the companion mass, and  $G$  is the gravitational constant. Assuming all the measurements can be approximated as representing the same orbital epoch, then combining these three equations gives

$$M_B = \frac{\rho^2 (a_{\alpha\delta}^2 + a_{RV}^2)^{3/2}}{\varpi^2 G a_{\alpha\delta}^2}. \quad (7)$$

If the errors on  $\rho$ ,  $a_{\alpha\delta}$ , and  $a_{RV}$  are small and Gaussian (and the error on parallax is negligible), we may use

standard propagation of errors to obtain

$$\frac{\sigma^2[M_B]}{M_B^2} \approx 4 \frac{\sigma^2[\rho]}{\rho^2} + 9 \frac{a_{RV}^2 \sigma^2[a_{RV}]}{(a_{RV}^2 + a_{\alpha\delta}^2)^2} + \left( 3 \frac{a_{\alpha\delta} \sigma[a_{\alpha\delta}]}{a_{RV}^2 + a_{\alpha\delta}^2} - 2 \frac{\sigma[a_{\alpha\delta}]}{a_{\alpha\delta}} \right)^2. \quad (8)$$

If the error on parallax is not negligible, it would have to also be propagated through the  $a_{\alpha\delta}$  terms, making Equation (8) slightly more involved. The parallax is needed to convert  $a_{\alpha\delta}$  from angular to linear units; its observational uncertainty is negligible for all systems studied here.

The difference between the *Gaia* DR2 proper motion and the *Hipparcos*–*Gaia* scaled positional difference provides our highest signal-to-noise ratio measurement of acceleration in the plane of the sky. This is not an instantaneous measurement, but is rather the difference between a mean proper motion over a baseline of  $\sim 25$  years and a mean proper motion during the *Gaia* observing period. For long-period systems like the ones we study here, we may take the latter proper motion to be effectively instantaneous. The central epoch of *Hipparcos* and *Gaia* is near 2003.5, while *Gaia* DR2 gives a nearly instantaneous measurement at an epoch close to 2015.5. In this section, we consider the accelerations in right ascension and declination to be measured at the same time, equal to the average of the two central epochs (we will drop this approximation when fitting orbits in the next section). Assuming nearly constant acceleration, we have

$$a_{\alpha\delta}[t_a] \sim \frac{\Delta\mu_{Gaia}}{(t_{Gaia} - t_{Hip})/2}, \quad (9)$$

with

$$t_a = \frac{3t_{Gaia} + t_{Hip}}{4}. \quad (10)$$

Table 3 lists the components of  $\Delta\mu_{Gaia}$  and the epochs of the two catalogs for our sample stars.

For  $a_{RV}$ , we fit a quadratic in date  $-(t_{Gaia} - t_{Hip})/2$  to the radial velocity data. We take the linear term and its standard error for  $a_{RV}$  and  $\sigma[a_{RV}]$  after adjusting the jitter to obtain a reduced  $\chi^2$  of unity. For Gl 86, we first subtract the best-fit radial velocity signal from the inner planet Gl 86b as determined in the following section. Finally, for the separation, we fit the functions

$$\Delta\alpha = b_0 + b_1 t + \frac{1}{2} \gamma t^2 a_\alpha \quad \text{and} \quad (11)$$

$$\Delta\delta = c_0 + c_1 t + \frac{1}{2} \gamma t^2 a_\delta \quad (12)$$

where  $t$  is the date relative to our desired epoch of  $t_a$ ,  $\sqrt{b_0^2 + c_0^2}$  is the separation at our desired epoch,  $a_\alpha$  and  $a_\delta$  are the stellar astrometric accelerations in right ascension and declination, and we expect  $\gamma = M_{\text{tot}}/M_B$ . We account for the errors in  $a_\alpha$  and  $a_\delta$  by first ignoring them and fitting for the coefficients, and then iteratively updating the covariance matrix with the previous  $\gamma$  and redoing the fit. We then numerically compute the covariance matrix of  $b_0$  and  $c_0$  about the best  $\chi^2$  to determine a standard error on separation at  $t_a$ .

Once we have approximate measurements at a single epoch, we apply Equations (7) and (8) to obtain approxi-

TABLE 3  
SUMMARY OF *Hipparcos* AND *Gaia* ASTROMETRY

Star	Data Source	$\Delta\mu_\alpha^\dagger$ (mas/yr)	$\sigma[\mu_\alpha]$	$\Delta\mu_\delta^\dagger$ (mas/yr)	$\sigma[\mu_\delta]$	Correlation Coefficient	Epoch, $\alpha$ year	Epoch, $\delta$ year
HD 4747	<i>Hip</i>	1.315	0.737	-5.118	0.588	0.067	1991.43	1991.67
	<i>Gaia</i>	3.067	0.552	-1.715	0.588	0.751	2015.20	2015.19
Gl 86	<i>Hip</i>	-15.072	0.428	12.726	0.463	-0.083	1991.23	1991.38
	<i>Gaia</i>	17.898	0.134	-3.528	0.115	-0.072	2015.77	2015.75
HD 68017	<i>Hip</i>	9.697	0.925	-5.444	0.524	-0.170	1991.07	1991.34
	<i>Gaia</i>	-13.017	0.159	-3.951	0.099	-0.219	2015.76	2015.71
Gl 758	<i>Hip</i>	0.616	0.475	1.432	0.447	-0.024	1990.97	1991.21
	<i>Gaia</i>	-0.386	0.061	-0.933	0.071	-0.036	2015.62	2015.67
HR 7672	<i>Hip</i>	-2.430	0.492	5.176	0.516	0.017	1991.32	1991.13
	<i>Gaia</i>	4.561	0.144	-7.080	0.144	0.095	2015.60	2015.64

$\dagger$  Defined as in Equation (3)

TABLE 4  
APPROXIMATE COMPANION MASSES FROM SHORT ORBITAL ARCS

Star	$\rho$ (mas)	$a_{\alpha\delta}$ (m s <sup>-1</sup> yr <sup>-1</sup> )	$a_{RV}$	$M_2$ ( $M_{Jup}$ )
Gl 86	2210 $\pm$ 18	76.5 $\pm$ 0.6	-61.0 $\pm$ 3.0 $\dagger$	512 $\pm$ 30 $\dagger$
HD 68017	655 $\pm$ 8	113.8 $\pm$ 1.2	6.77 $\pm$ 0.35	129 $\pm$ 3
Gl 758	1875 $\pm$ 18	6.10 $\pm$ 0.42	-2.44 $\pm$ 0.16	37 $\pm$ 2

$\dagger$  The best-fit planet signal from Section 6 has been subtracted off.

mate masses with error bars for the objects in our sample with long orbital periods. Table 4 shows our results. We achieve a typical formal precision of  $\sim 5\%$  even for systems with orbital periods of more than a century. However, our assumptions in deriving the equations of this section are not fully satisfied for the three systems in Table 4, and are not at all satisfied by HD 4747 and HR 7672. In general, a finite difference measurement of the astrometric acceleration will tend to underestimate the instantaneous acceleration. This is particularly true if the orbital period is only a few times larger than the *Hipparcos-Gaia* temporal baseline. As a result, the values in Table 4 systematically underestimate the true masses. While this section demonstrates *why* we can obtain excellent companion masses, full orbit fits are necessary to obtain accurate constraints.

## 6. ORBIT FITTING

The previous section shows that precise masses are possible with a nearly instantaneous measurement of the three-dimensional acceleration and projected separation. However, all of the systems presented here trace out a non-negligible fraction of the orbit over the *Hipparcos-Gaia* baseline. We therefore perform full orbit fitting of our combined astrometric and RV data sets in a way similar to Bowler et al. (2018), with the main difference being that we include the astrometric acceleration between *Hipparcos* and *Gaia* DR2.

We use the parallel-tempering Markov chain Monte Carlo (PT-MCMC) ensemble sampler in *emcee* v2.1.0 (Foreman-Mackey et al. 2013) that is based on the algorithm described by Earl & Deem (2005). Our results are based on the “coldest” of 30 chains, where the “hottest” chain effectively samples all of the allowed parameter space. We use 100 walkers to sample our 11-parameter model over  $2 \times 10^5$  steps. Two of these parameters are the masses of the host ( $M_\star$ ) and companion ( $M_{comp}$ ). Six

parameters define the orbit: semimajor axis ( $a$ ), inclination ( $i$ ), PA of the ascending node ( $\Omega$ ), mean longitude at a reference epoch ( $t_{ref}$ ) of 2455197.5 JD ( $\lambda_{ref}$ ; 2010 Jan 1 00:00 UT), and finally eccentricity ( $e$ ) and the argument of periastron ( $\omega$ ) fitted as  $\sqrt{e} \sin \omega$  and  $\sqrt{e} \cos \omega$ . Two additional orbit parameters are needed for the RV data set to define the zero point of the system velocity ( $RV_{zero}$ ) and the intrinsic jitter ( $\sigma_{jit}$ ). Lastly, we include parallax ( $\varpi$ ) as a fitted parameter in order to impose a Gaussian prior based on the DR2 measurement and its formal error. We assume log-flat priors for  $a$ ,  $M_\star$ ,  $M_{comp}$ , and  $\sigma_{jit}$ , a prior of  $\sin i$  for inclination, and uniform priors for all other fitted parameters. For objects with RV data sets from more than one instrument, we use two additional parameters for  $RV_{zero}$  and  $\sigma_{jit}$  for each extra instrument. The final likelihood used in our MCMC is

$$\ln \mathcal{L} = -0.5 (\chi_\rho^2 + \chi_\theta^2 + \chi_{RV}^2 + \chi_\varpi^2 + \chi_G^2 + \chi_H^2) + \ln [\sin[i]] - \ln[a] - \ln[M_\star] - \ln[M_{comp}] \quad (13)$$

with

$$\chi_\rho^2 = \sum_{k=1}^{N_{ast}} \frac{(\rho_k - \rho[t_k])^2}{\sigma^2[\rho_k]} \quad (14)$$

$$\chi_\theta^2 = \sum_{k=1}^{N_{ast}} \frac{(\arctan[\sin[\theta_k - \theta[t_k]], \cos[\theta_k - \theta[t_k]]])^2}{\sigma^2[\theta_k]} \quad (15)$$

$$\chi_{RV}^2 = \sum_{j=1}^{N_{inst}} \sum_{k=1}^{N_{RV}} \frac{(RV_{rel,k} + RV_{zero,j} - RV[t_k])^2}{\sigma^2[RV_k] + \sigma_{jit,j}^2} + \sum_{j=1}^{N_{inst}} \sum_{k=1}^{N_{RV}} \ln[\sigma^2[RV_k] + \sigma_{jit,j}^2] \quad (16)$$

$$\chi_\varpi^2 = \frac{(\varpi - \varpi_{DR2})^2}{\sigma^2[\varpi_{DR2}]} \quad (17)$$

$$\chi_G^2 = (\Delta\mu_{\alpha,G} - \Delta\mu_{\alpha,G'})^2 C_{\alpha\alpha,G}^{-1} + (\Delta\mu_{\delta,G} - \Delta\mu_{\delta,G'})^2 C_{\delta\delta,G}^{-1} + 2(\Delta\mu_{\alpha,G} - \Delta\mu_{\alpha,G'}) (\Delta\mu_{\delta,G} - \Delta\mu_{\delta,G'}) C_{\alpha\delta,G}^{-1} \quad (18)$$

$$\begin{aligned}
\chi_H^2 = & (\Delta\mu_{\alpha,H} - \Delta\mu_{\alpha,H'})^2 C_{\alpha\alpha,H}^{-1} \\
& + (\Delta\mu_{\delta,H} - \Delta\mu_{\delta,H'})^2 C_{\delta\delta,H}^{-1} \\
& + 2 (\Delta\mu_{\alpha,H} - \Delta\mu_{\alpha,H'}) (\Delta\mu_{\delta,H} - \Delta\mu_{\delta,H'}) C_{\alpha\delta,H}^{-1}
\end{aligned} \tag{19}$$

In Equations (18) and (19),  $\Delta\mu_{\alpha,G'}$ ,  $\Delta\mu_{\delta,G'}$ ,  $\Delta\mu_{\alpha,H'}$  and  $\Delta\mu_{\delta,H'}$  refer to a model orbit’s differences between the proper motion at either the *Gaia* DR2 epoch near 2015.5 or the *Hipparcos* epoch near 1991.25 and the mean proper motion between the *Hipparcos* and *Gaia* epochs. The  $C^{-1}$  of Equations (18) and (19) are the relevant elements of the inverse of the covariance matrix; the covariance matrices themselves are computed from the uncertainties and correlations listed in Table 3. We omit the  $\ln \sigma^2$  factors from all of the equations above apart from Equation (16) for the radial velocities. The jitter parameters  $\sigma_{\text{jit},j}^2$  are the only uncertainties we vary in our MCMC; the other variances are constants and do not affect the relative likelihood of two sets of parameters.

When modeling the orbits, we attempt to account for the fact that *Hipparcos* and *Gaia* do not provide truly instantaneous proper motions. We calculate the proper motions  $\Delta\mu_{\alpha,G'}$ ,  $\Delta\mu_{\delta,G'}$ ,  $\Delta\mu_{\alpha,H'}$  and  $\Delta\mu_{\delta,H'}$  using a quadratic fit to the star’s modeled position, centered on the epoch provided by the HGCA and with a time baseline corresponding to the 3.4-year duration of *Hipparcos* or the 22 months of *Gaia* DR2, as appropriate.

For Gl 86, the RV data set includes a signal from the close-in Jupiter-mass planet, so we include five more parameters in our orbit model: orbital period ( $P_{\text{pl}}$ ), mean longitude at  $t_{\text{ref}}$  ( $\lambda_{\text{ref,pl}}$ ), eccentricity ( $e_{\text{pl}}$ ) and argument of periastron ( $\omega_{\text{pl}}$ ) fitted as  $\sqrt{e_{\text{pl}}} \sin \omega_{\text{pl}}$  and  $\sqrt{e_{\text{pl}}} \cos \omega_{\text{pl}}$ , and the RV semiamplitude of the planet’s orbit ( $K_{1,\text{pl}}$ ). We assume log-flat priors on  $P_{\text{pl}}$  and  $K_{1,\text{pl}}$  and uniform priors on the other three parameters.

In our PT-MCMC analysis, we have experimented with different chain lengths. We found that after  $2 \times 10^5$  steps our 100-walker chains had stabilized in the mean and rms of the posteriors of each of the model parameters for all objects analyzed. We saved every 50th step of our chains and discarded the first 75% of the chain as the burn-in portion, leaving  $10^5$  PT-MCMC samples in the cold chain. Tables 5–9 list information on the posterior distributions of our fitted parameters, as well as parameters that can be directly computed from them. The 1- and 2- $\sigma$  confidence intervals are computed as the minimum range in that parameter that contains 68.3% and 95.4% of the values, respectively. The best-fit solution quoted is the one with the maximum posterior probability density (likelihood times prior).

Figure 4 shows the relative orbits of all systems on the sky. Figures 5, 9, 13, 17, and 21 display the companion mass posterior and the most relevant parameter correlations; Figures 6, 10, 14, 18, and 22 display all other marginalized parameter posteriors. Figures 7, 11, 15, 19, 23 show the RV orbits over the full period of the best-fit orbit as well as zoomed in plots of each RV data set. Figures 8, 12, 16, 20, and 24 show the relative astrometry and astrometric accelerations compared to our orbit fits. In all of the aforementioned figures, the best-fit orbit is shown as a thick, black line, and 100 randomly drawn orbits from the MCMC posterior are plotted as thin lines

colored according to the corresponding companion mass from low mass (pink) to high mass (green).

## 7. RESULTS AND DISCUSSION

In this section we discuss the results of our orbital fits to each star. For each of the systems except HD 4747, the mass of the secondary has the tightest constraint (for HD 4747 it is the orbital period). For Gl 758B, HD 68017B, and Gl 86B, these masses represent major improvements on the constraints available in the literature.

For the three ultracool dwarfs in our sample, we also compare our dynamical masses to the predictions of some commonly-used brown dwarf models. Our substellar cooling models are Cond (Baraffe et al. 2003), the models of Saumon & Marley (2008) with three different cloud treatments, and the Burrows et al. (1997) grid. The three families of models from Saumon & Marley (2008) have no clouds (“SM-NC”), a shift in cloud cover at the L/T transition (“SM-Hybrid”), or thick clouds at all temperatures (“SM-f2”). We use the age posteriors derived from both stellar activity and isochrone fits, the green dot-dashed curves in the lower-middle panels of Figure 2. Probability distributions of age and bolometric luminosity combine with a given brown dwarf cooling model to provide the model-derived mass distributions.

Figure 3 shows our results. We obtain good agreement between dynamical and model-derived masses for all of our systems for at least one model, although some models show better agreement than others.

### 7.1. HD 4747

HD 4747B is an excellent test case for our method because its orbit has been studied extensively in previous work. Our dynamical mass of  $m = 66.2_{-3.0}^{+2.5} M_{\text{Jup}}$  is in reasonable agreement with published values of  $m = 65.3_{-3.3}^{+4.4} M_{\text{Jup}}$  (Crepp et al. 2018) and  $m = 70.2 \pm 1.6 M_{\text{Jup}}$  (Peretti et al. 2018) that had to assume a mass for the host star. We find a dynamical mass for HD 4747A of  $M = 0.82_{-0.08}^{+0.07} M_{\odot}$  that agrees well with published isochrone analysis as well as our own. The  $\chi^2$  of the best-fit orbit compared to the input astrometric measurements indicates a good fit and accurate measurement errors, with values of 7.39 and 5.89 for separations and PAs (eight measurements each) and 3.09 for the four proper motion differences.

Our orbital parameters are generally in good agreement with the results of Peretti et al. (2018) and somewhat discrepant with Crepp et al. (2018). This is most likely because we used the same relative astrometry as Peretti et al. (2018), and they noted the same differences in orbital parameters compared to Crepp et al. (2018) that we find. Despite this fact, our companion mass  $m = 66.2_{-3.0}^{+2.5} M_{\text{Jup}}$  agrees better with the  $m = 65.3_{-3.3}^{+4.4} M_{\text{Jup}}$  found by Crepp et al. (2018) than the  $m = 70.2 \pm 1.6 M_{\text{Jup}}$  derived by Peretti et al. (2018). Our best-fit *sini* differs by 5% from that found by Peretti et al. (2018), accounting for most of the discrepancy in mass and illustrating the importance of including the *Hipparcos–Gaia* acceleration. Our model-independent dynamical mass has somewhat larger errors (4%) compared to the 2.3% mass of Peretti et al. (2018). This may

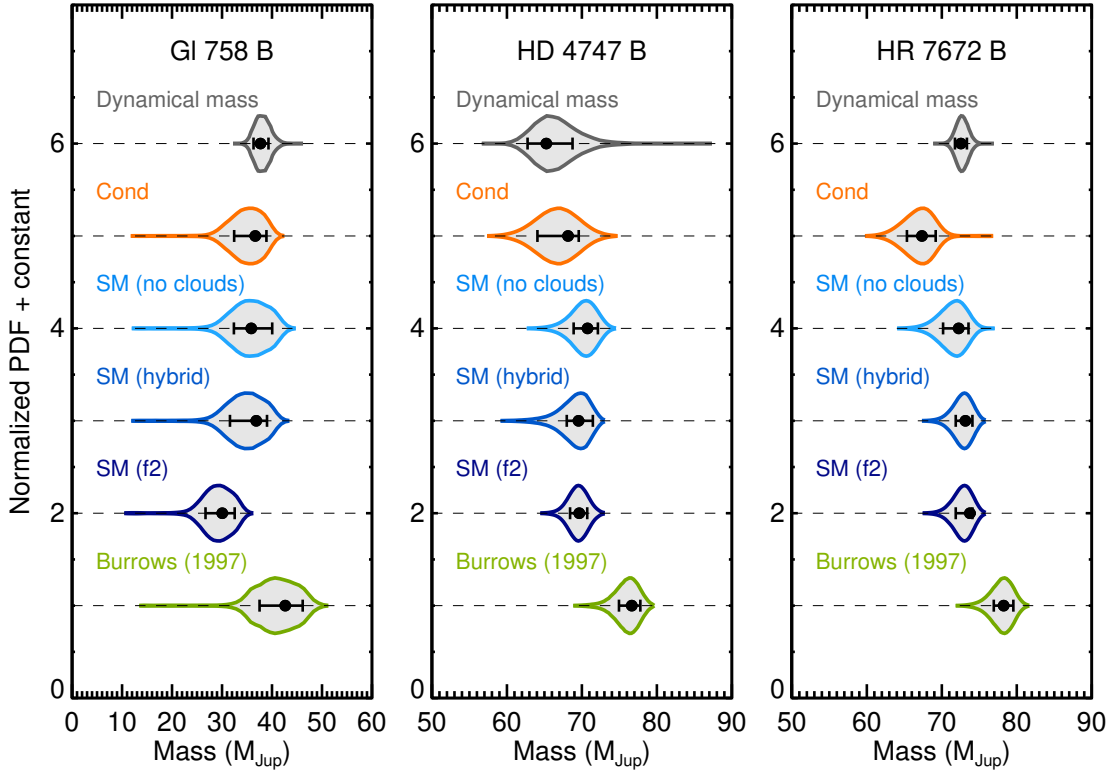


FIG. 3.— Comparison of the dynamical masses of our ultracool dwarfs with masses inferred from the companion’s age and bolometric luminosity using a range of substellar cooling models. We adopt the activity+isochrone age posteriors, the dot-dashed green curves from the lower-middle panels of Figure 2. The brown dwarf evolution models are Cond (Baraffe et al. 2003), Saumon & Marley (2008) with three treatments of clouds, and Burrows et al. (1997). For each object, at least one substellar cooling model agrees well with our dynamical mass measurement. This good agreement for Gl 758B is in contrast to some earlier results, and is due to our low measured mass and old inferred age.

be a consequence of fitting for the host star mass directly rather than using an isochronal mass.

HD 4747AB has the shortest orbital period of any of the systems in our sample ( $34.0^{+0.8}_{-1.0}$  yr), but its period is still much longer than either the *Hipparcos* or *Gaia* mission duration. The period is comparable to the temporal baseline between the missions, resulting in a large astrometric signal. This star also has low precision in *Gaia*, perhaps because it heavily saturated the *Gaia* CCDs. Despite this, our results for HD 4747 demonstrate the ability of *Hipparcos* and *Gaia* to measure dynamical masses of systems with periods of only a few decades. HD 4747 will be an excellent test case for future *Gaia* data releases, which will both measure a larger fraction of the orbit and improve the processing for very bright stars.

Figure 3 compares the dynamical mass of HD 4747B with mass predictions from theoretical models based on the objects age and luminosity. We adopt the age posterior derived using both stellar activity and isochrone fitting. Our bolometric luminosity of  $\log[L_{\text{bol}}/L_{\odot}] = -4.54 \pm 0.06$  dex is derived using the  $K_s$ -band absolute magnitude of Crepp et al. (2016) together with the empirical magnitude–luminosity of Dupuy & Liu (2017) based on the luminosities of Filippazzo et al. (2015). All of the brown dwarf cooling models except for those of Burrows et al. (1997) provide consistent masses within the errors.

## 7.2. Gl 86

The significance of proper motion acceleration in the difference between *Gaia* proper motion for Gl 86 and the scaled *Hipparcos*–*Gaia* positional difference is over  $130\sigma$ . Even at such a high significance, the formal goodness-of-fit is excellent for relative and absolute astrometry, making Gl 86 a robust demonstration of the power of using *Hipparcos* and *Gaia* astrometry to determine orbits.

Thanks to the  $>100\sigma$  significance of acceleration in *Hipparcos* and *Gaia*, we obtain a mass on Gl 86B of  $0.595 \pm 0.010 M_{\odot}$ , better than 2% precision. This model-independent mass is broadly consistent with the dynamical analysis of Lagrange et al. (2006), who found a possible range in mass of  $0.48\text{--}0.62 M_{\odot}$ , and our orbital eccentricity of  $0.53^{+0.04}_{-0.03}$  is consistent with their conclusion that  $e > 0.4$ . Our mass is also consistent with the value of  $0.59 \pm 0.01 M_{\odot}$  derived in the photometric and spectroscopic analysis of Gl 86B by Farihi et al. (2013). According to their analysis, this mass implies a progenitor mass of  $1.9 \pm 0.1 M_{\odot}$ , main sequence lifetime of  $1.4 \pm 0.2$  Gyr, and cooling age of  $1.25 \pm 0.05$  Gyr. A total system age of 2.7 Gyr agrees well with our stellar age for Gl 86A, and Farihi et al. (2013) also noted that it agrees with the age–activity relationship of Mamajek & Hillenbrand (2008). In contrast, Fuhrmann et al. (2014) noted the tension between such a young age and the chemistry and kinematics of Gl 86A, which they determined was inter-

mediate between the thin and thick disks implying an age of  $\sim 10$  Gyr. Such an old age would require a lower-mass progenitor, and thus a lower mass for the white dwarf of  $0.49 \pm 0.02 M_{\odot}$ . Our model-independent mass for the white dwarf seems to be inconsistent with the scenario proposed by Fuhrmann et al. (2014), but the chemical and kinematic peculiarity of Gl 86A calls for further study.

Some caution is still warranted in using dynamical masses that rely on relative astrometry from different instruments that have been calibrated to varying levels of accuracy (HST/WFC3, VLT/NACO, and ADONIS/SHARPII here). For example, Bowler et al. (2018) found that even instruments thought to be well-calibrated sometimes delivered astrometry in disagreement with each other, but that was only evident when there were many degrees of freedom (many measurements per instrument). This is not the case for Gl 86, where each literature source provides only one or a few measurements. Given that Gl 86 has the highest *precision* of all our masses, it is worth noting that it may not have comparable *accuracy* due to the heterogeneous relative astrometry used in our orbit analysis.

### 7.3. HD 68017

HD 68017 represents the second highest-mass companion and the second highest signal-to-noise ratio in the *Hipparcos-Gaia* catalog of the objects we study here. We obtain a dynamical mass of  $0.147 \pm 0.003 M_{\odot}$  for the secondary. Our  $\chi^2$  for the absolute astrometry provided by *Hipparcos* and *Gaia* is somewhat high at 9.6 for four measurements. It is difficult to assign a number of degrees of freedom to the absolute astrometry, as the parameters are jointly constrained by absolute and relative astrometry and by radial velocities. For four degrees of freedom, a  $\chi^2$  value of 9.6 occurs about 5% of the time.

Our adopted separation uncertainties are inflated over the values published by Crepp et al. (2012b), but are still much lower than the uncertainties of 5 mas ultimately adopted by Bowler et al. (2018) for their orbital fit of Gl 758B. Those authors added 4.3 mas in quadrature with their uncertainties to achieve a reduced  $\chi^2$  of unity on the relative astrometry. Adding a similar amount of uncertainty to our separation would allow for a satisfactory fit to the *Hipparcos* and *Gaia* astrometry. Because the system is accelerating through the *Hipparcos* and *Gaia* measurements, the exact measured proper motions will also depend somewhat on the distribution of astrometric epochs.

Crepp et al. (2012b) originally estimated the mass of HD 68017B from isochrones ( $0.16 \pm 0.02 M_{\odot}$ , Dotter et al. 2008) and an empirical mass relation ( $0.15 \pm 0.01 M_{\odot}$ , Delfosse et al. 2000). Our dynamical mass is in excellent agreement with these values and will help refine the mass–metallicity–magnitude relation in the future given that it is a companion to a metal-poor G dwarf ( $[\text{Fe}/\text{H}] = -0.44 \pm 0.03$  dex, Crepp et al. 2012b).

### 7.4. Gl 758

Our mass of  $m = 38.1^{+1.7}_{-1.5} M_{\text{Jup}}$  for Gl 758B, obtained with the aid of the cross-calibrated astrometric catalog of Brandt (2018), significantly improves previous constraints. Bowler et al. (2018) obtained a mass

of  $m = 42^{+19}_{-7} M_{\text{Jup}}$  from the same companion astrometry and radial velocity measurements that we use but assuming a host star mass prior of  $0.97 \pm 0.02 M_{\odot}$ . Calissendorff & Janson (2018) refined this constraint to  $m = 42.4^{+5.6}_{-5.0} M_{\text{Jup}}$  by using the *Hipparcos* and *Gaia* DR2 proper motions and Bowler et al. (2018) posteriors. They did not, however, use the scaled positional difference (the most precise proper motion measurement), nor did they cross-calibrate the *Hipparcos* and *Gaia* catalogs.

Our mass is firmly on the low end of that determined by Bowler et al. (2018), consistent with their lower mass limit, as well as Calissendorff & Janson (2018). In Section 2, we show that the activity and rotation of Gl 758A favor an age  $\gtrsim 6$  Gyr, while isochrone fitting, depending on the band(s) used, is consistent with any age. We favor both an older system age and a lower companion mass than previous work, eliminating much of the tension with evolutionary models of brown dwarfs. Figure 3 demonstrates that Cond, the Burrows et al. (1997) models, and the Saumon & Marley (2008) models (apart from those with thick clouds at all temperatures) all make predictions consistent with our dynamical mass and age posteriors.

Gl 758B is the lowest luminosity brown dwarf ( $\log[L_{\text{bol}}/L_{\odot}] = -6.07 \pm 0.03$  dex, Bowler et al. 2018) for which a precise dynamical mass has been measured, as the sample of Dupuy & Liu (2017) extends to  $-5.0$  dex, and the components of  $\epsilon$  Ind B (Dieterich et al. 2018) have luminosities of  $-4.71$  dex and  $-5.35$  dex (King et al. 2010).

### 7.5. HR 7672

HR 7672B has a previous dynamical mass of  $m = 68.7^{+2.4}_{-3.1} M_{\text{Jup}}$  measured from radial velocities and relative astrometry (Crepp et al. 2012a). As such, it presents another excellent test case of our method, like HD 4747B. HR 7672B passed close to its host star in projection around 2015 (Figure 4), as predicted by Crepp et al. (2012a); this results in proper motion changing sign within the time frame of *Gaia* observations (see Figure 24). We obtain a dynamical mass of  $m = 72.7 \pm 0.8 M_{\text{Jup}}$  for HR 7672B,  $1.6\sigma$  higher than Crepp et al. (2012a). We also find somewhat higher eccentricity and longer orbital period for the orbit. HR 7672A has the most precise dynamical mass among the host stars in our sample,  $0.96^{+0.04}_{-0.05} M_{\odot}$ , which is somewhat lower than the value of  $1.08 \pm 0.04 M_{\odot}$  inferred from the star’s color and luminosity and used in the Crepp et al. (2012a) dynamical analysis. There is not significant correlation between companion mass and other parameters like eccentricity and period in our MCMC posteriors (Figure 21), so it is not apparent why our mass for the companion is systematically higher than that of Crepp et al. (2012a).

Our best-fit orbit for HR 7672 is suspiciously good in separation and position angle, suggesting that errors in relative astrometry may have been overestimated. The  $\chi^2$  in position angle, for example, is just 0.55 for six measurements. The best-fit orbit is poorer for the host-star astrometry, with  $\chi^2$  of 11.4 for our four proper motion measurements. Such a discrepancy is expected 2.2% of the time in a  $\chi^2$  distribution with four degrees of freedom. If we attribute the discrepancy to systematics in the catalog or to the heavy tails in the low-precision *Gaia*

proper motions, and inflate uncertainties beyond the calibrations of the Brandt (2018) catalog, it may increase the uncertainty on our dynamical mass. Underestimated uncertainties or unaccounted systematics in the Liu et al. (2002) astrometry could also explain the relatively poor fit to the calibrated *Hipparcos* and *Gaia* astrometry.

Our best-fit mass for HR 7672B is very close to the hydrogen burning limit, placing this object near the stellar/substellar boundary. We derive a bolometric luminosity of  $\log[L_{\text{bol}}/L_{\odot}] = -4.14 \pm 0.06$  dex by combining the  $K_s$ -band photometry of Boccaletti et al. (2003) with the calibrations of Dupuy & Liu (2017), or  $\log[L_{\text{bol}}/L_{\odot}] = -4.23 \pm 0.05$  dex using  $H$ -band photometry. Figure 3 adopts the weighted average of these two values,  $\log[L_{\text{bol}}/L_{\odot}] = -4.19 \pm 0.04$  dex. This bolometric luminosity falls within the range that Dupuy & Liu (2017) identified as the end of the main sequence ( $10^{-4.3} - 10^{-3.9} L_{\odot}$ ). Evolutionary models from Saumon & Marley (2008) predict that an object with the luminosity and mass of HR 7672B is still cooling but that it will eventually stabilize on the main sequence once it reaches an age of several Gyr. Our best-fit mass is marginally consistent with the Cond (Baraffe et al. 2003) and Burrows et al. (1997) models; it agrees well with the cooling curves of Saumon & Marley (2008) regardless of the assumptions about cloud cover.

## 8. CONCLUSIONS

In this paper, we have combined the astrometric catalog of Brandt (2018) with radial velocities and relative astrometry to determine absolute orbits and thereby measure model-independent dynamical masses. The astrometric catalog represents a cross-calibration of *Hipparcos* and *Gaia* DR2, including an assessment of systematic errors needed to bring the two catalogs in agreement, constructed with the goal of joint orbit fitting in mind. We choose an initial sample of five objects: three ultracool dwarfs, one white dwarf, and one low-mass star. We also perform a uniform age analysis on all five of the host stars.

For our two more massive ultracool dwarfs, HD 4747B and HR 7672B, we determine more precise dynamical masses that improve on and are consistent with previous results, notably using no external constraints on the host star masses. Both of these brown dwarfs lie near or below the hydrogen burning limit, and both are intermediate in age ( $\sim 2$ – $4$  Gyr based on activity-age relations and isochrone fitting). For Gl 758B, the lowest-luminosity imaged brown dwarf with a dynamical mass, we significantly improve on previously determined masses (Bowler et al. 2018; Calissendorff & Janson 2018). The latter authors used *Hipparcos* and *Gaia* astrometry but without performing a cross-calibration between the two catalogs and without using the scaled position difference (i.e., the proper motion between *Hipparcos* and *Gaia* epochs computed from the reported catalog RA and Dec positions). Our mass of  $38.1^{+1.7}_{-1.5} M_{\odot}$  for Gl 758B is firmly on the low end of previous determinations and on the high end of the original estimate from Thalmann et al. (2009). Our mass, combined with an older host-star age ( $\gtrsim 6$  Gyr), resolves previous apparent discrepancies and is consistent with predictions from brown dwarf cooling models.

For the white dwarf Gl 86B, we find a dynamical mass

of  $0.595 \pm 0.010 M_{\odot}$  that sheds light on the progenitor star’s history. Our mass is consistent with the spectroscopic and photometric analysis of this white dwarf companion by Farihi et al. (2013), who found that the progenitor star was massive ( $1.9 \pm 0.1 M_{\odot}$ ) with a relatively short main sequence lifetime ( $1.4 \pm 0.2$  Gyr) and subsequent white dwarf cooling time ( $1.25 \pm 0.05$  Gyr). This scenario is also consistent with our activity-based age of the host star. However, our mass is inconsistent with the scenario proposed by Fuhrmann et al. (2014), who noted that the chemistry and kinematics of Gl 86A imply a much older age that would require a lower mass progenitor and lower mass white dwarf ( $0.49 \pm 0.02 M_{\odot}$ ). The present-day orbit we determine will also inform the formation history of this system where the lower-mass star in the system (Gl 86A) formed a massive planet (Gl 86b).

Finally, we measure a precise mass for the low-mass star HD 68017B of  $0.147 \pm 0.003 M_{\odot}$  in good agreement with previous estimates based on its absolute magnitude. As a rare example of an M dwarf with a low-metallicity ( $[\text{Fe}/\text{H}] = -0.44 \pm 0.03$  dex) and precisely measured dynamical mass, HD 68017B will help constrain the mass–magnitude–metallicity relation in the future.

Our analysis here can serve as a prototype for further dynamical masses derived using the Brandt (2018) catalog. By combining the absolute astrometry from this catalog with data for well-characterized companions, we have quantitatively vetted the errors reported in the catalog for stars with significant acceleration detections. Thousands of stars show astrometric acceleration, and many of the companions responsible for these accelerations will be amenable to direct imaging and dynamical mass measurements. Model-independent masses of stars, brown dwarfs, and white dwarfs will provide new anchors to theoretical models of their formation and evolution.

The authors thank the anonymous referee for a thorough and helpful report. Some of the data presented herein were obtained at the W. M. Keck Observatory, which is operated as a scientific partnership among the California Institute of Technology, the University of California and the National Aeronautics and Space Administration. The Observatory was made possible by the generous financial support of the W. M. Keck Foundation. The authors wish to recognize and acknowledge the very significant cultural role and reverence that the summit of Maunakea has always had within the indigenous Hawaiian community. We are most fortunate to have the opportunity to conduct observations from this mountain. This work has made use of data from the European Space Agency (ESA) mission *Gaia* (<https://www.cosmos.esa.int/gaia>), processed by the Gaia Data Processing and Analysis Consortium (DPAC, <https://www.cosmos.esa.int/web/gaia/dpac/consortium>). Funding for the DPAC has been provided by national institutions, in particular the institutions participating in the *Gaia* Multilateral Agreement. T.D.B. gratefully acknowledges support from the Heising-Simons foundation and from NASA under grant #80NSSC18K0439. T.J.D. acknowledges research support from Gemini Observatory.

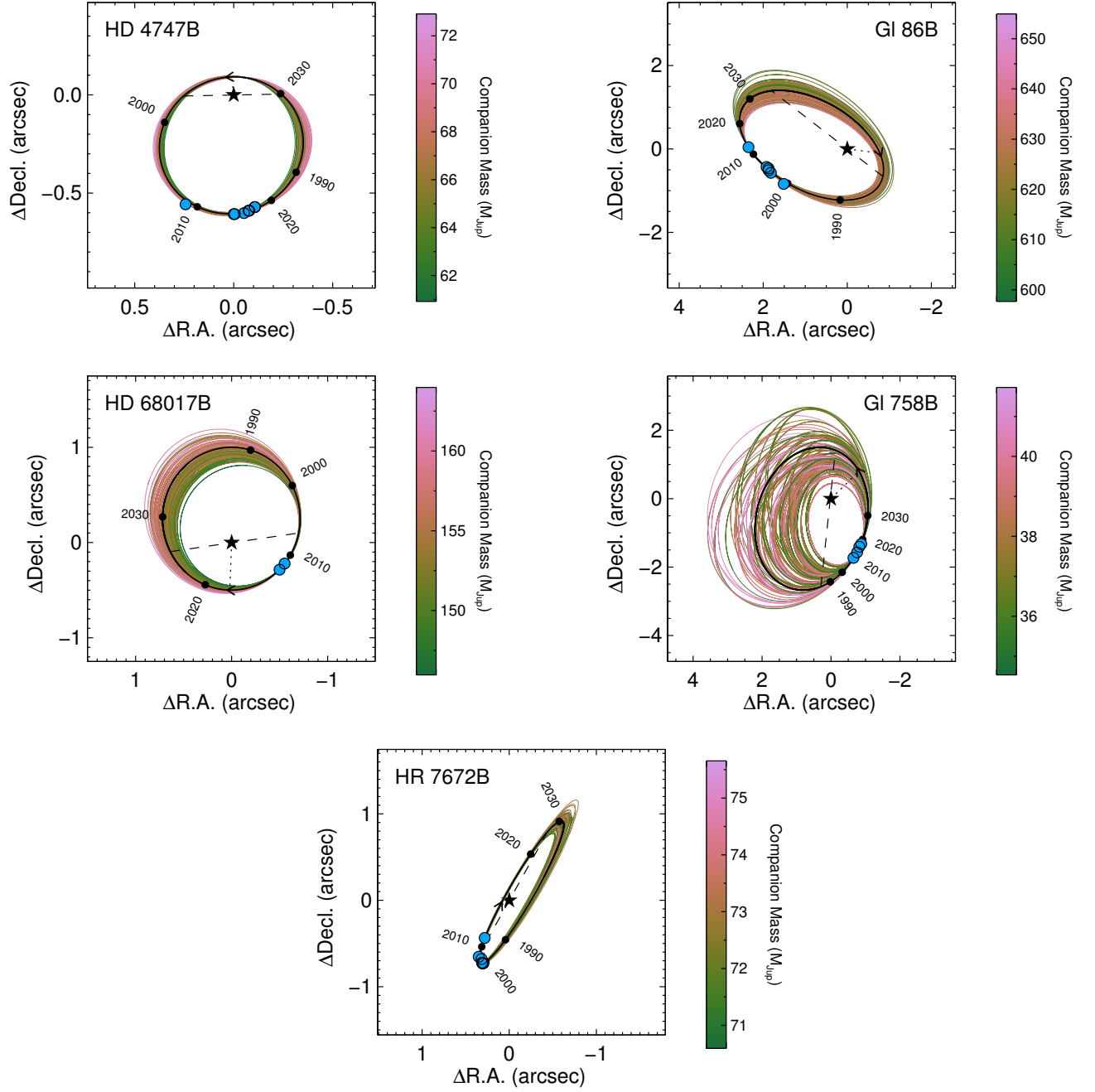


FIG. 4.— Relative astrometric orbits of companions. The thick black line is the highest likelihood orbit and thin lines are 100 orbits drawn randomly from our posterior distribution colored according to companion mass from pink (low mass) to green (high mass). Dotted lines connect the host star to the periastron passage. Arrows plotted at periastron passage indicate orbital direction. Dashed lines indicate the line of nodes, that is the intersection of orbital and sky planes. Past and future points along the orbit are indicated by small black dots. Relative astrometry measurements are plotted as larger filled circles, where measurement errors are typically smaller than the plotted symbols.

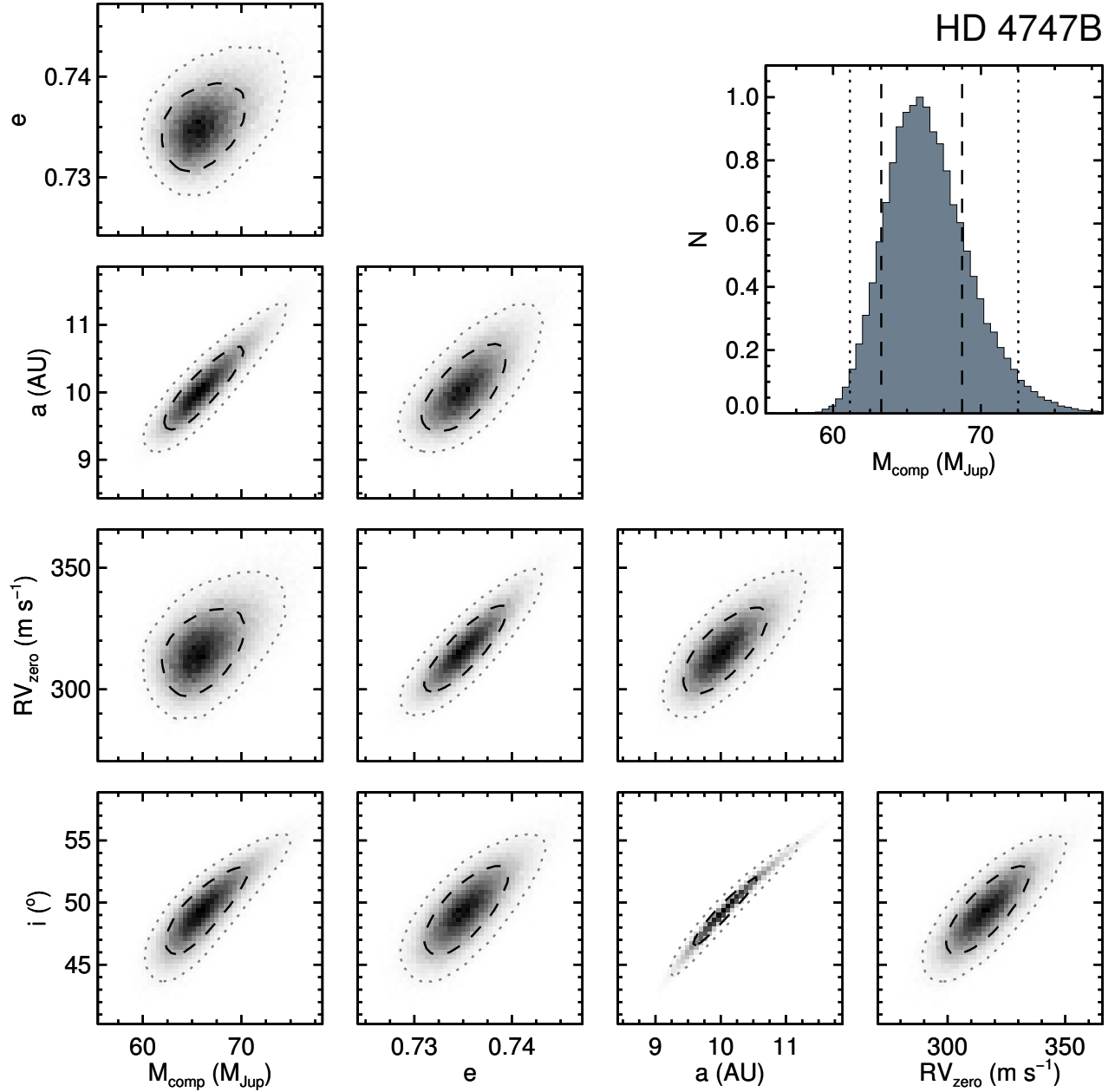


FIG. 5.— Joint posterior distributions for selected orbital parameters. Dark dashed contours indicate  $1\sigma$  ranges and lighter dotted contours indicate  $2\sigma$  ranges. The top right panel shows the posterior distribution of the companion's mass.



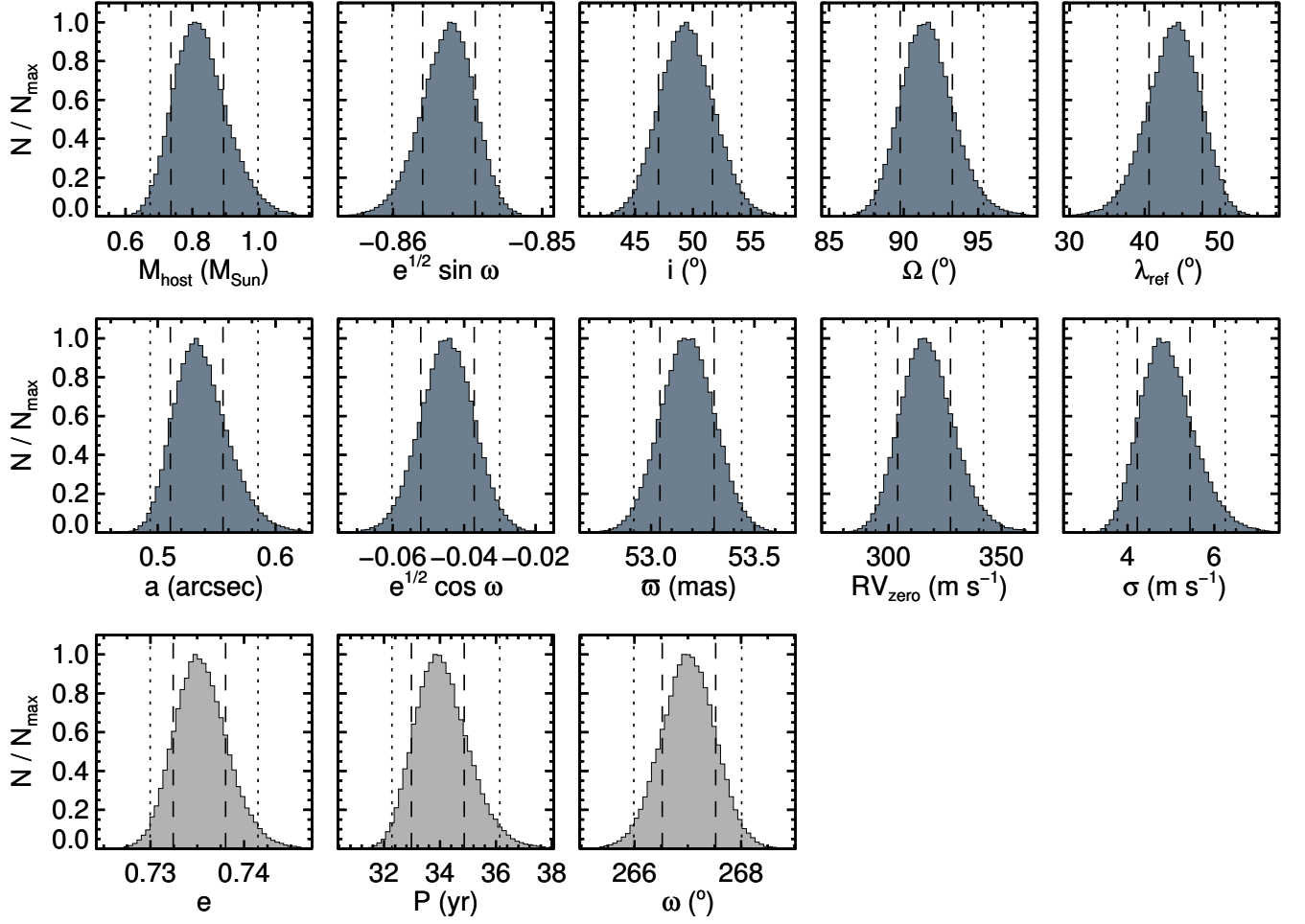


FIG. 6.— Marginalized posterior distributions for all directly fitted orbital parameters (dark gray histograms), aside from companion mass which is shown in Figure 5. Posteriors for properties computed from the directly fitted parameters are shown in light gray histograms.

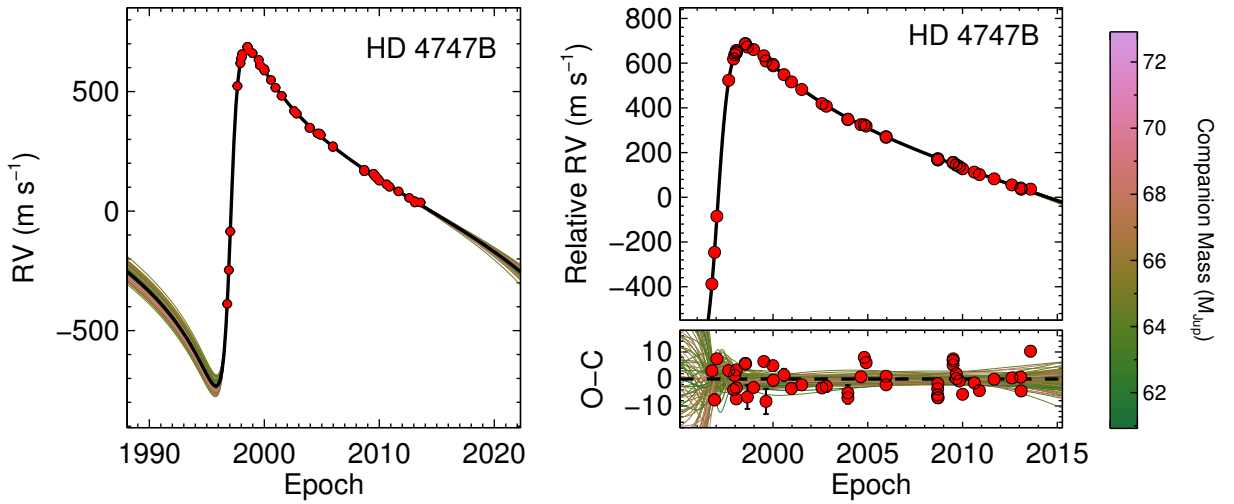


FIG. 7.— Left: The RV orbit induced by the directly imaged companion over a full orbital period, where the thick black line is the highest likelihood orbit and the thin lines are 100 orbits drawn randomly from our posterior distribution. These orbits are colored according to companion mass from pink (low mass) to green (high mass). RV measurements of the host star with the best-fit RV zero point added in are overlaid. RV of zero on this panel is the system’s barycentric velocity. Right: RV orbit induced by the directly imaged companion over the time range sampled by RV measurements. The zero point is arbitrary here as we plot relative RV measurements. The bottom panel shows residuals after subtracting the RV orbit from the measurements. Error bars are too small to be visible except for some points on the plot of residuals.

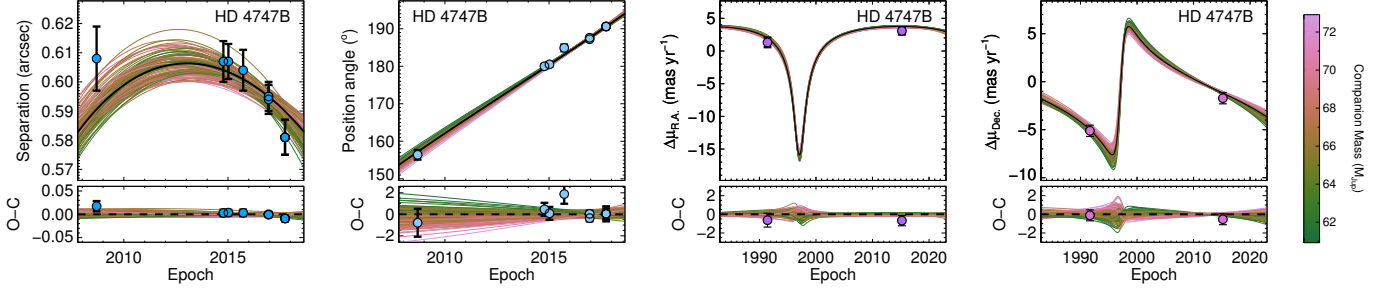


FIG. 8.— Top: astrometry of the directly imaged companion relative to the host star. Bottom: acceleration induced by the companion on the host star as measured from absolute astrometry from Hipparcos and Gaia. This acceleration is plotted in the same way as it is used in our orbital analysis, that is the difference between the instantaneous linear motion of the host star at a given epoch (Hipparcos and Gaia DR2) as compared to the proper motion computed from the position differences between those two epochs. In every panel, the thick black line is the highest likelihood orbit and the thin lines are 100 orbits drawn randomly from our posterior distribution. These orbits are colored according to companion mass from pink (low mass) to green (high mass).

TABLE 5  
MCMC ORBITAL POSTERiors FOR HD 4747B

Property	Median $\pm 1\sigma$	95.4% c.i.	Prior
Fitted parameters			
Companion mass $M_{\text{comp}} (M_{\text{Jup}})$	$66.2^{+2.5}_{-3.0}$	61.1, 72.5	$1/M$ (log-flat)
Host-star mass $M_{\text{host}} (M_{\odot})$	$0.82^{+0.07}_{-0.08}$	0.67, 1.00	$1/M$ (log-flat)
Parallax (mas)	$53.18 \pm 0.13$	52.92, 53.44	$\exp[-0.5((\varpi - \varpi_{\text{DR2}})/\sigma[\varpi_{\text{DR2}}])^2]$
Semimajor axis $a$ (AU)	$10.1^{+0.4}_{-0.5}$	9.3, 11.0	$1/a$ (log-flat)
Inclination $i$ ( $^{\circ}$ )	$49.4^{+2.3}_{-2.4}$	44.9, 54.2	$\sin(i)$ , $0^{\circ} < i < 180^{\circ}$
$\sqrt{e} \sin \omega$	$-0.8563^{+0.0018}_{-0.0017}$	-0.8601, -0.8528	uniform
$\sqrt{e} \cos \omega$	$-0.045^{+0.008}_{-0.007}$	-0.060, -0.030	uniform
Mean longitude at $t_{\text{ref}} = 2455197.5$ JD, $\lambda_{\text{ref}}$ ( $^{\circ}$ )	$44^{+4}_{-3}$	36, 51	uniform
PA of the ascending node $\Omega$ ( $^{\circ}$ )	$91.5^{+1.7}_{-1.8}$	88.1, 95.4	uniform
RV zero point ( $\text{m s}^{-1}$ )	$317^{+11}_{-13}$	294, 342	uniform
RV jitter $\sigma$ ( $\text{m s}^{-1}$ )	$4.9^{+0.6}_{-0.7}$	3.8, 6.3	$1/\sigma$ (log-flat)
Computed properties			
Orbital period $P$ (yr)	$34.0^{+0.8}_{-1.0}$	32.3, 36.1	...
Semimajor axis (mas)	$535^{+20}_{-25}$	494, 585	...
Eccentricity $e$	$0.7353^{+0.0027}_{-0.0029}$	0.7300, 0.7415	...
Argument of periastron $\omega$ ( $^{\circ}$ )	$267.0 \pm 0.5$	266.0, 268.0	...
Time of periastron $T_0 = t_{\text{ref}} - P \frac{\lambda - \omega}{360^{\circ}}$ (JD)	$2450471 \pm 5$	2450460, 2450482	...
Mass ratio $q = M_{\text{comp}}/M_{\text{host}}$	$0.077^{+0.004}_{-0.005}$	0.069, 0.086	...

NOTE. — The  $\chi^2$  of relative astrometry is 7.69 for separations and 6.82 for PAs, with 8 measurements for each. The  $\chi^2$  of the Hipparcos and Gaia proper motion differences is 3.09 for four measurements.

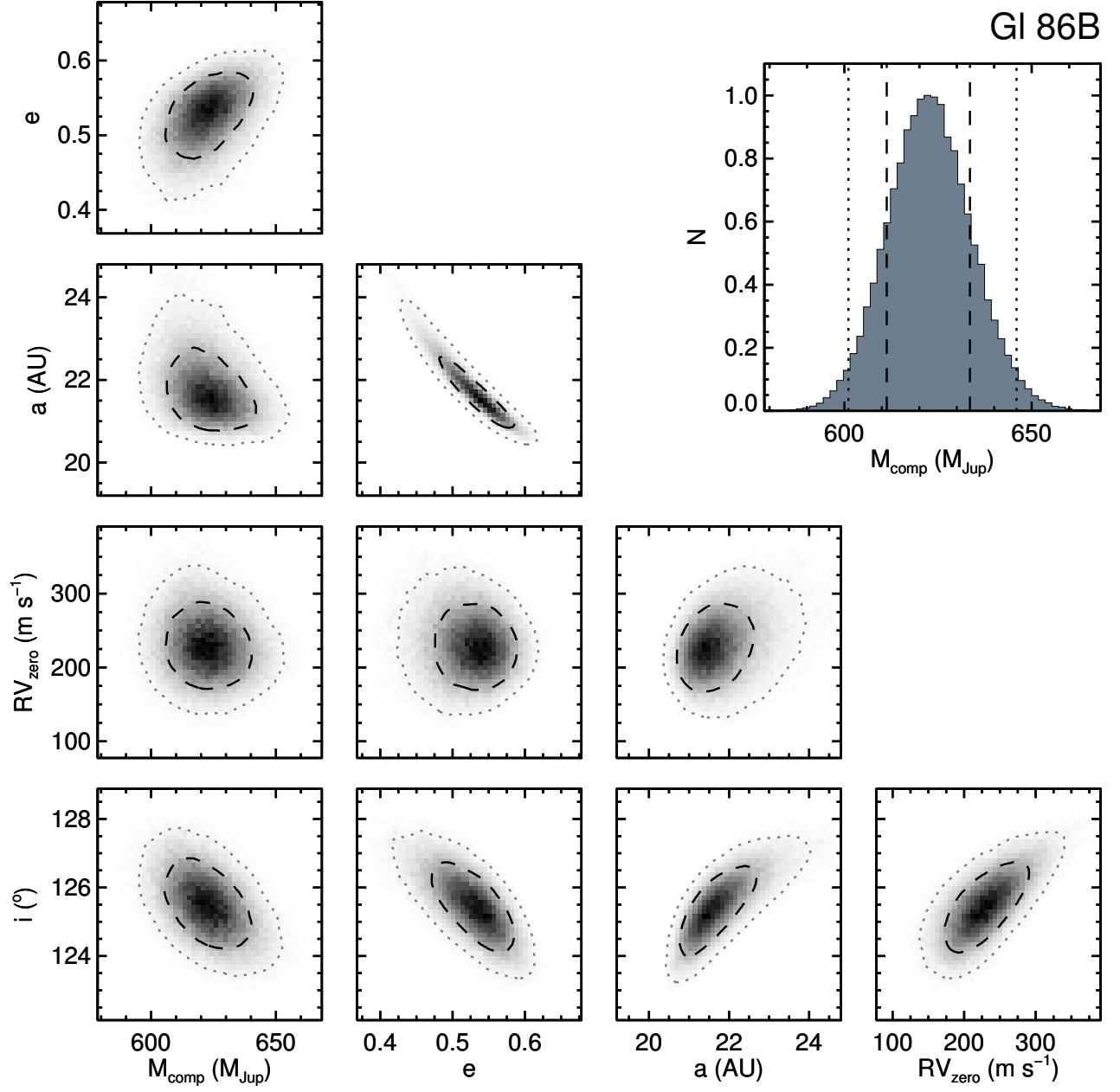


FIG. 9.— Same as Figure 5.

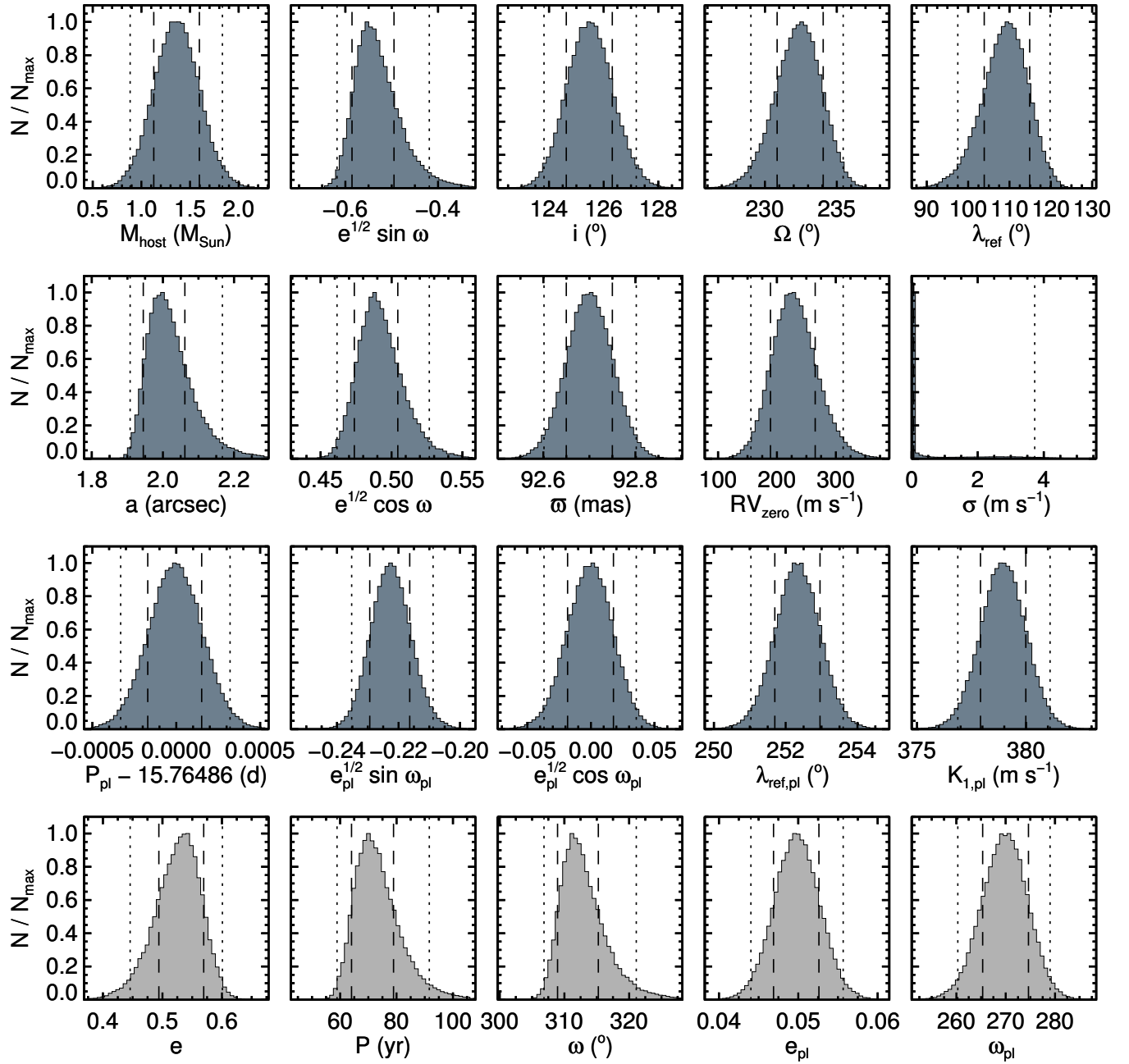


FIG. 10.— Same as Figure 6.

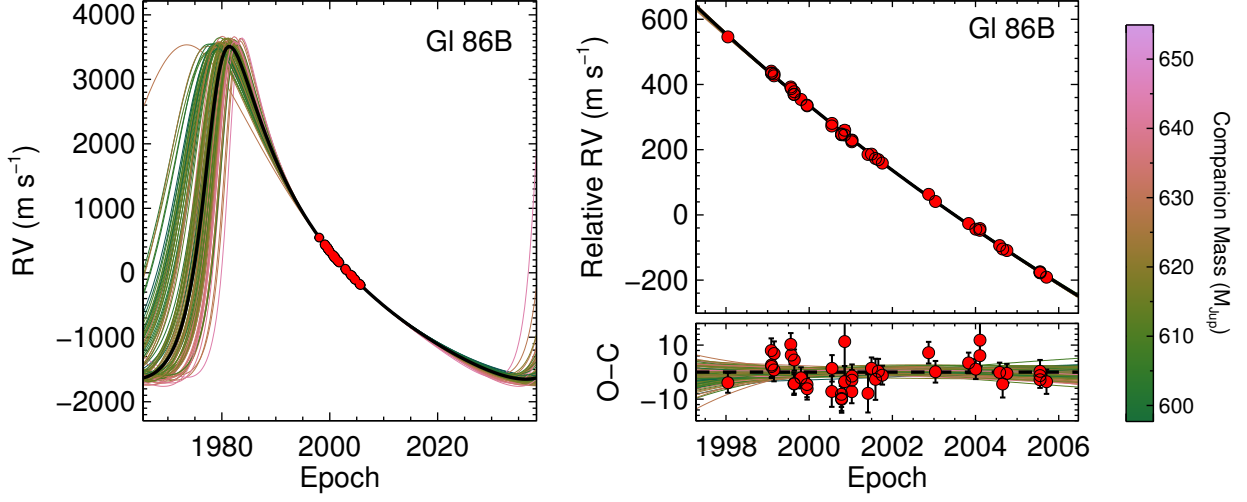


FIG. 11.— Same as Figure 7, and here the orbit of the inner planet GI 86 b has been subtracted off of the measured RVs.

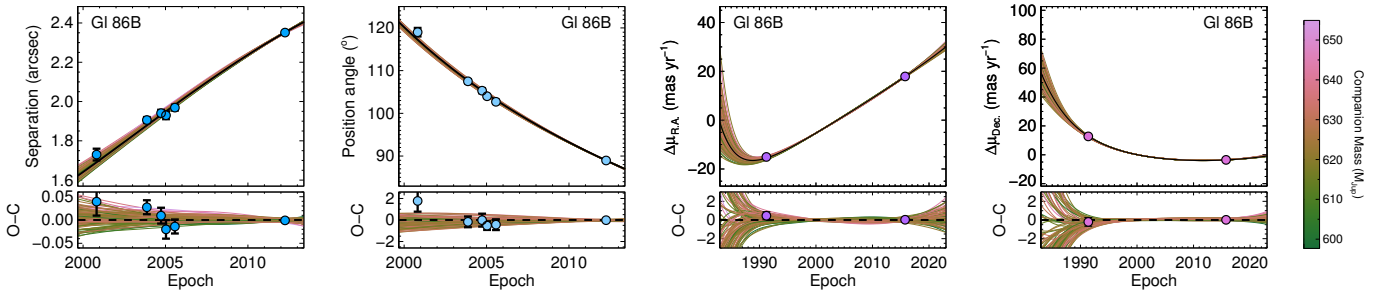


FIG. 12.— Same as Figure 8.

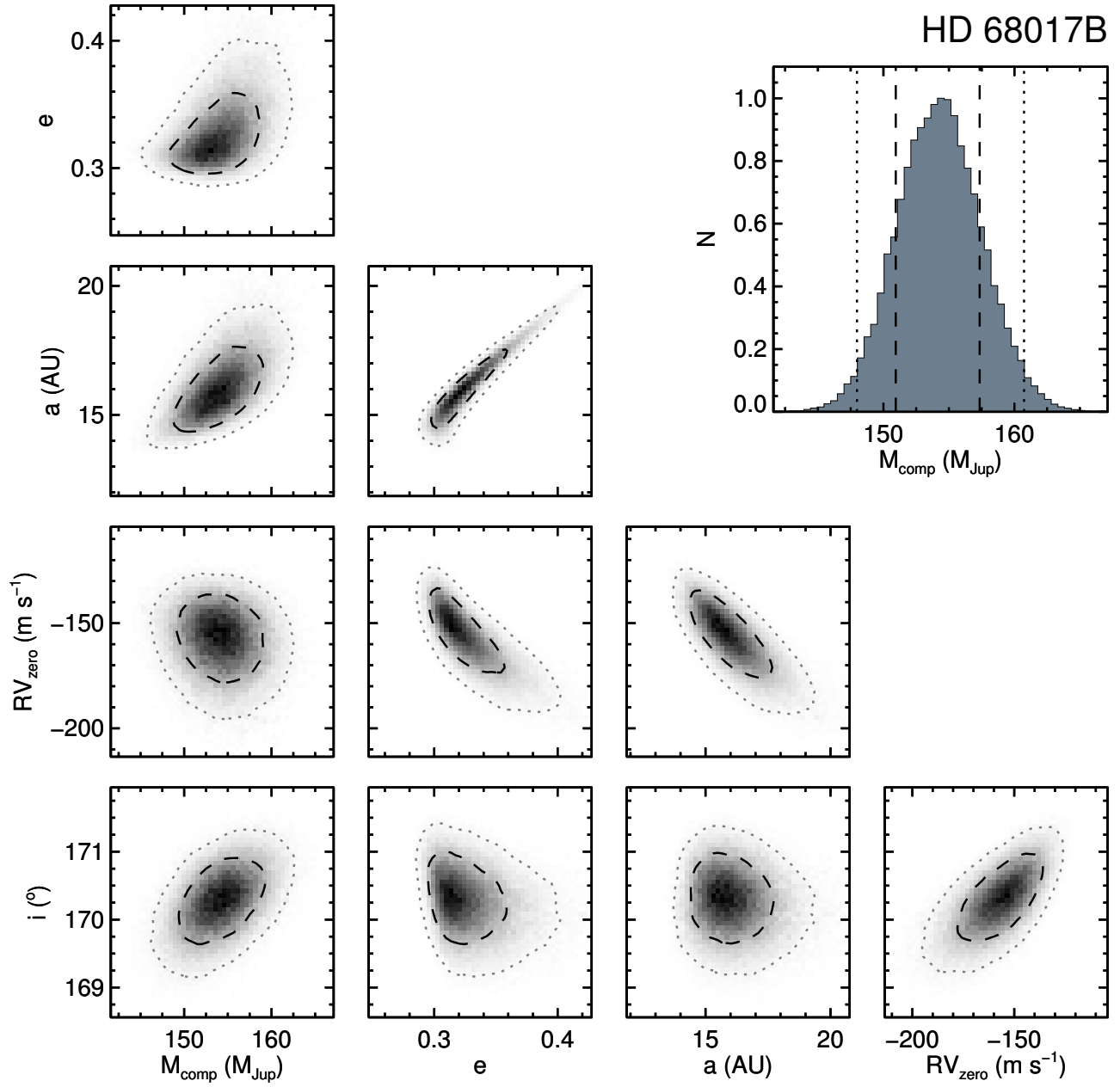


FIG. 13.— Same as Figure 5.

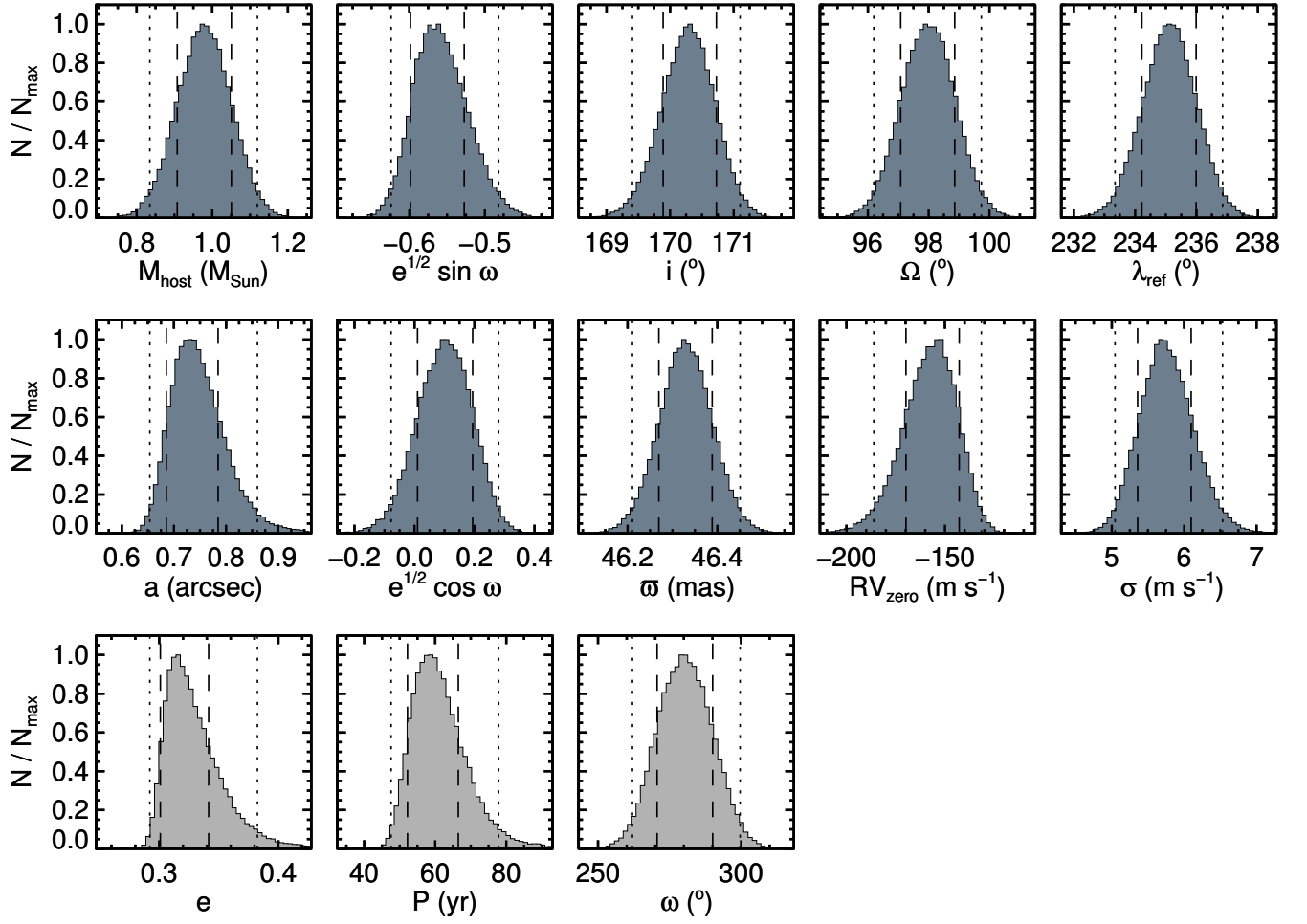


FIG. 14.— Same as Figure 6.

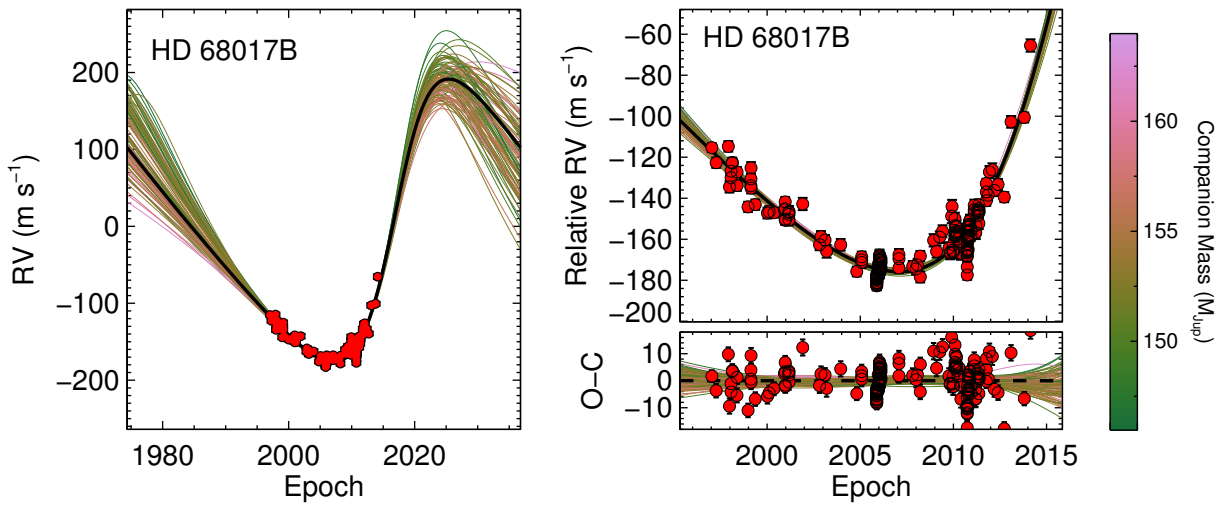


FIG. 15.— Same as Figure 7.

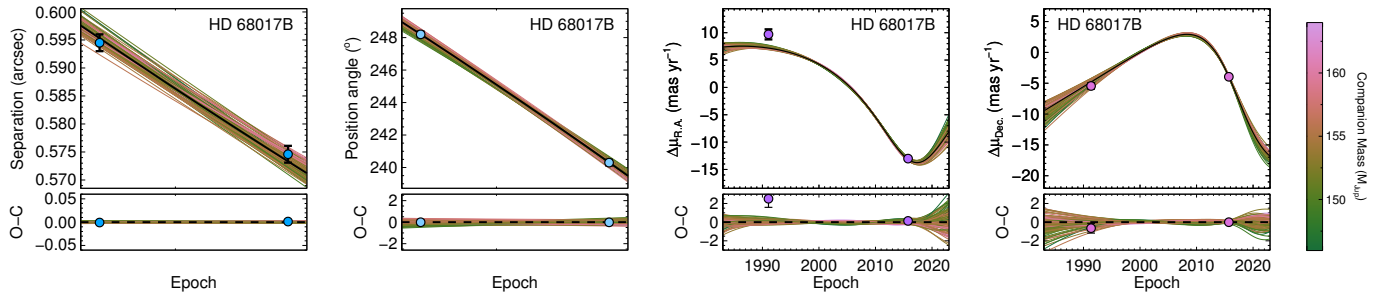


FIG. 16.— Same as Figure 8.

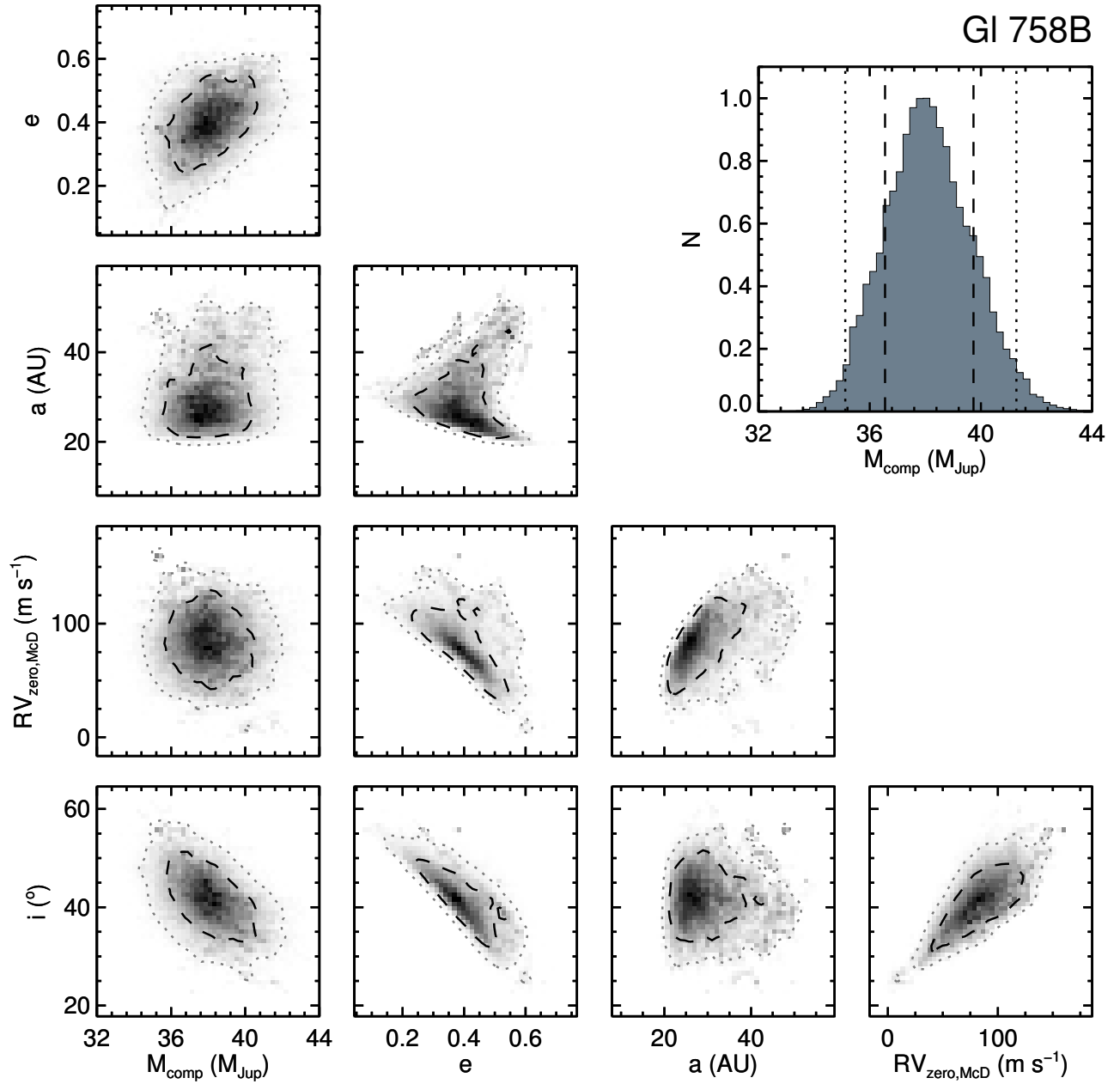


FIG. 17.— Same as Figure 5.



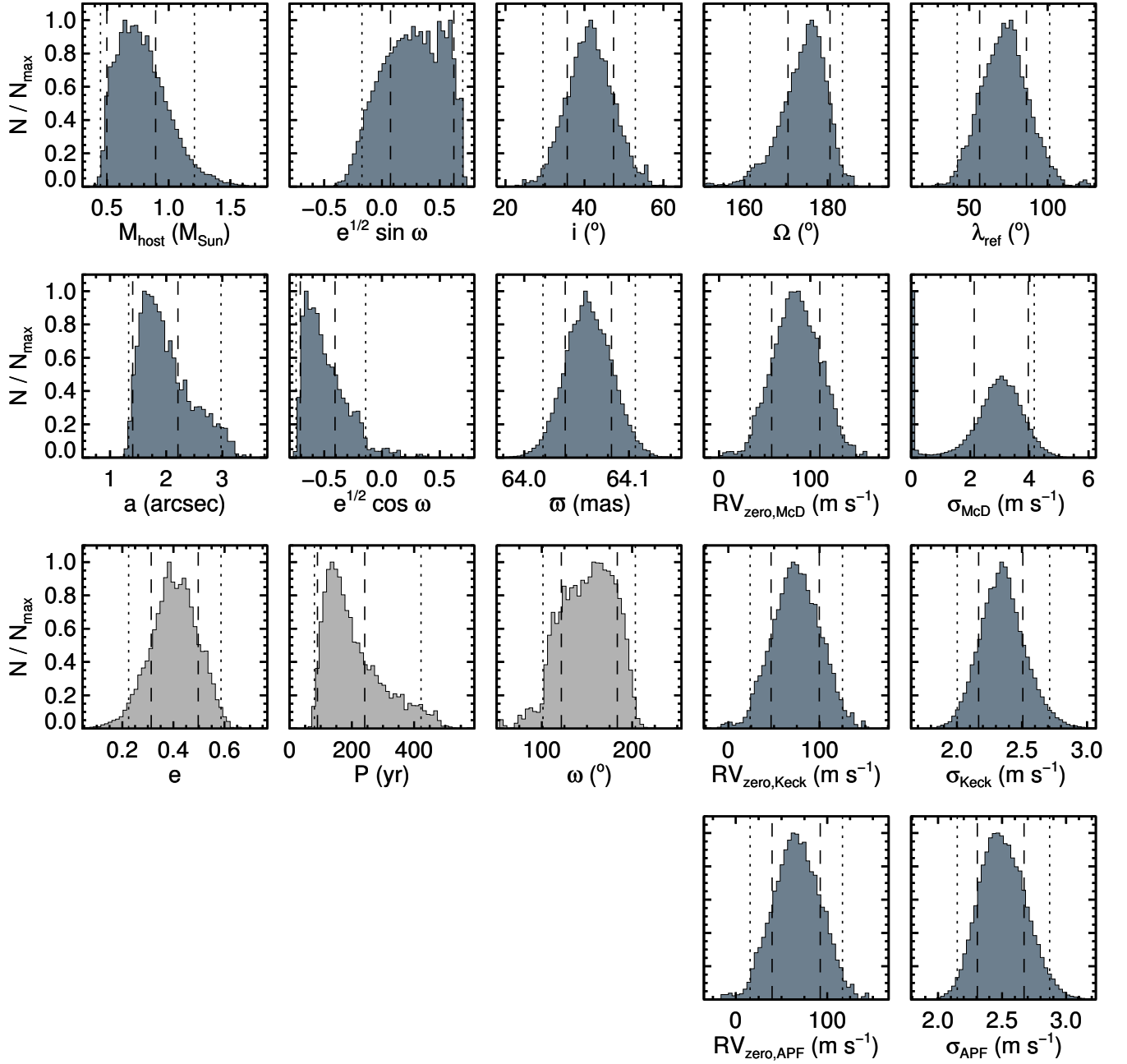


FIG. 18.— Same as Figure 6.

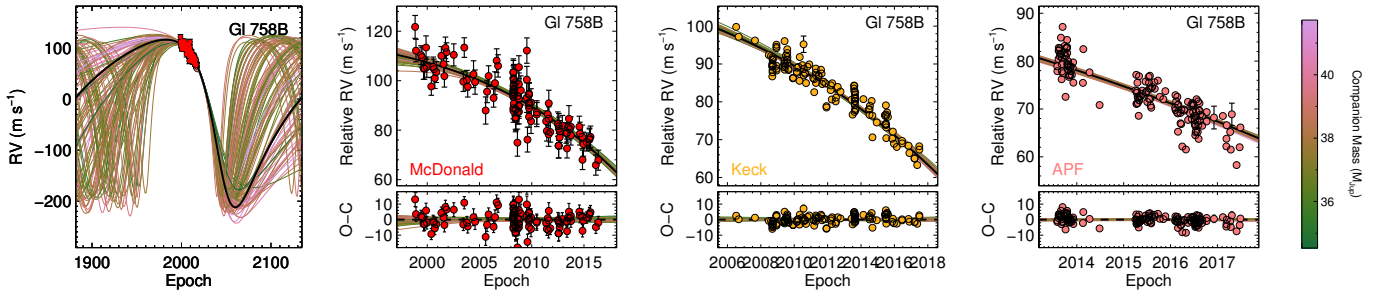


FIG. 19.— Same as Figure 7.

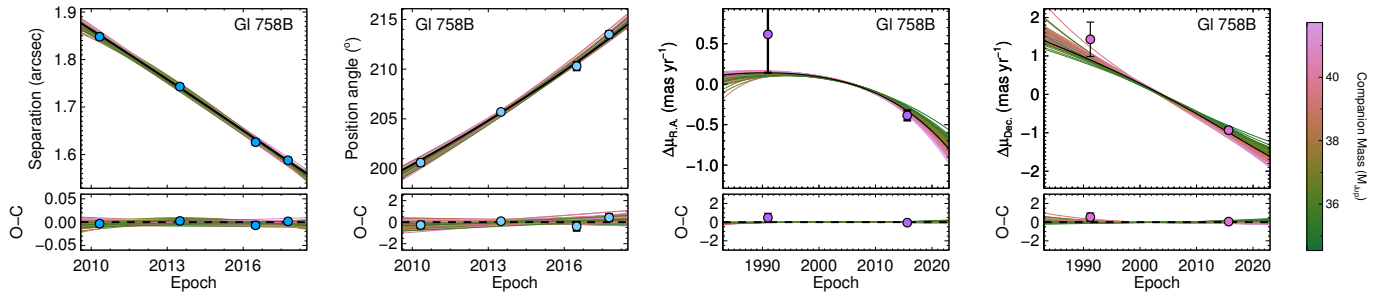


FIG. 20.— Same as Figure 8.

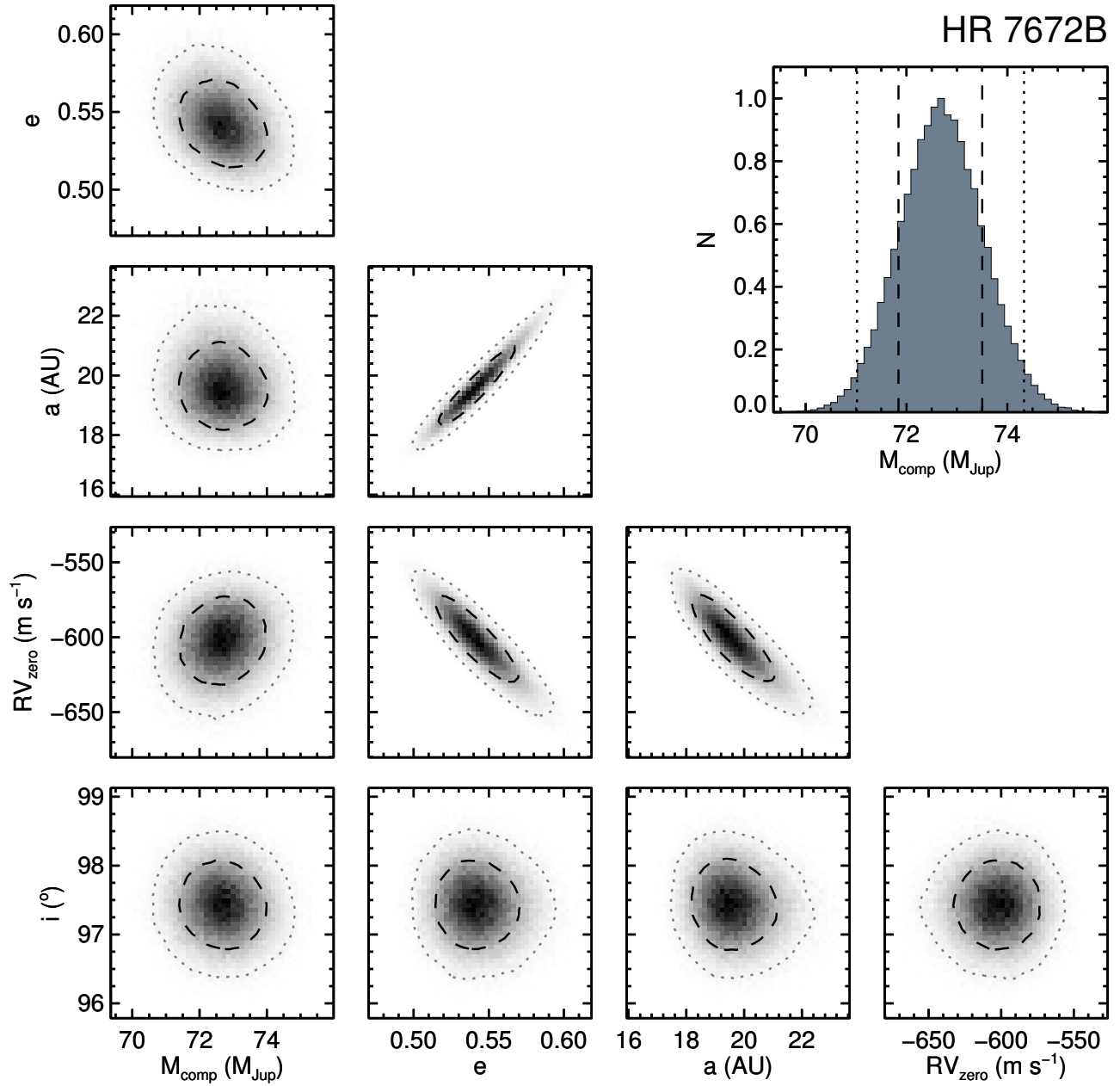


FIG. 21.— Same as Figure 5.

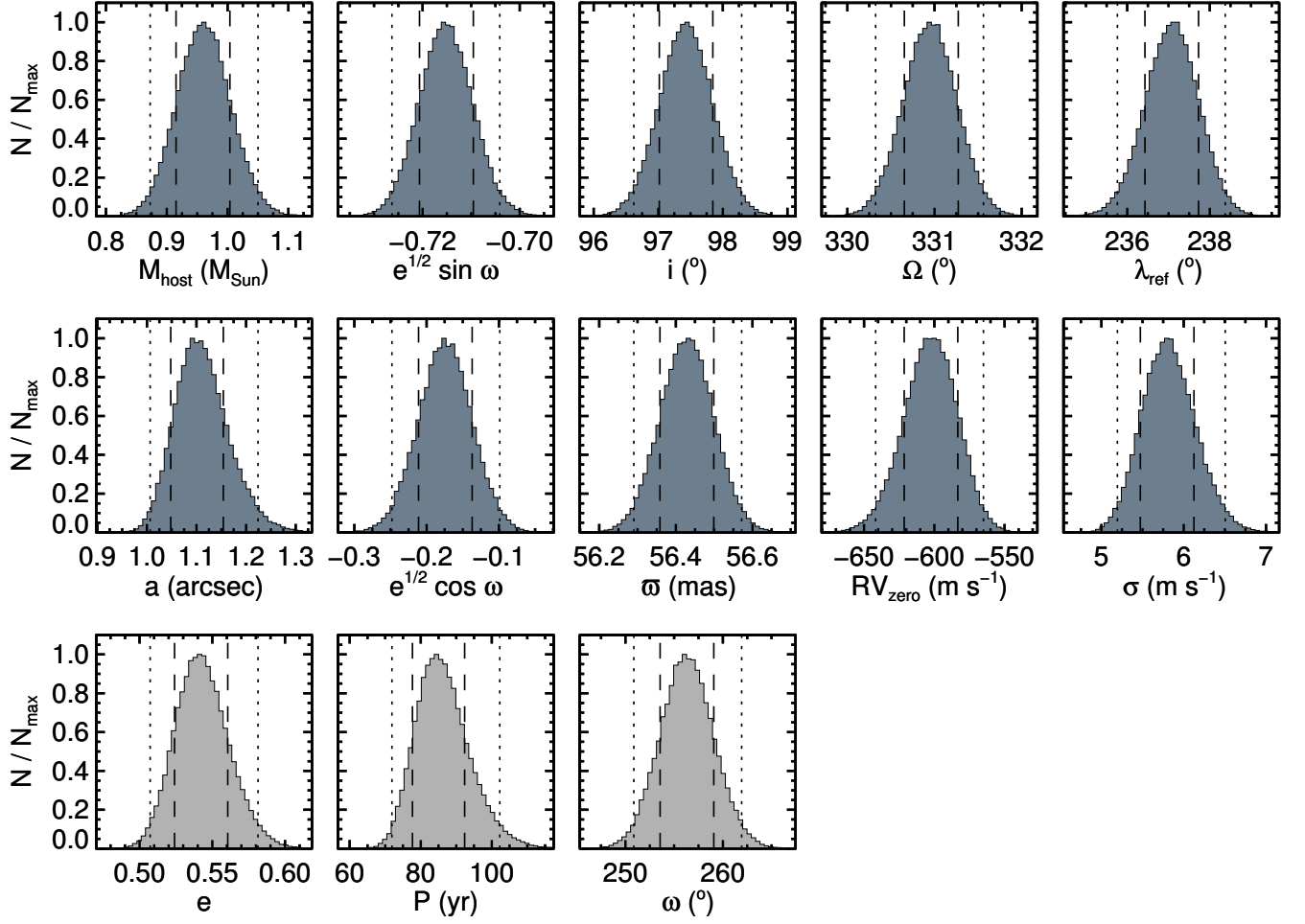


FIG. 22.— Same as Figure 6.

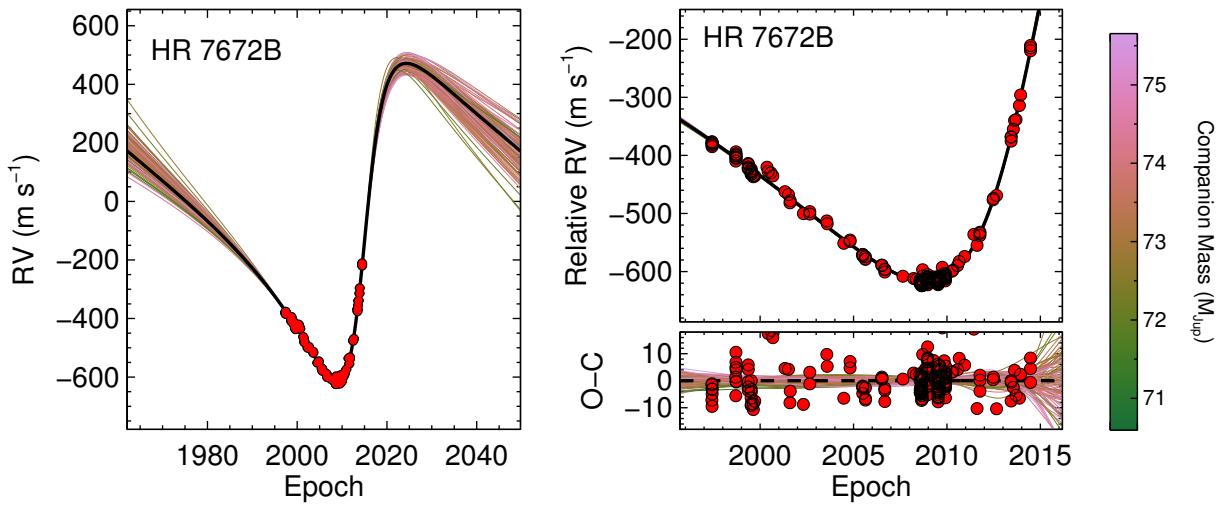


FIG. 23.— Same as Figure 7.

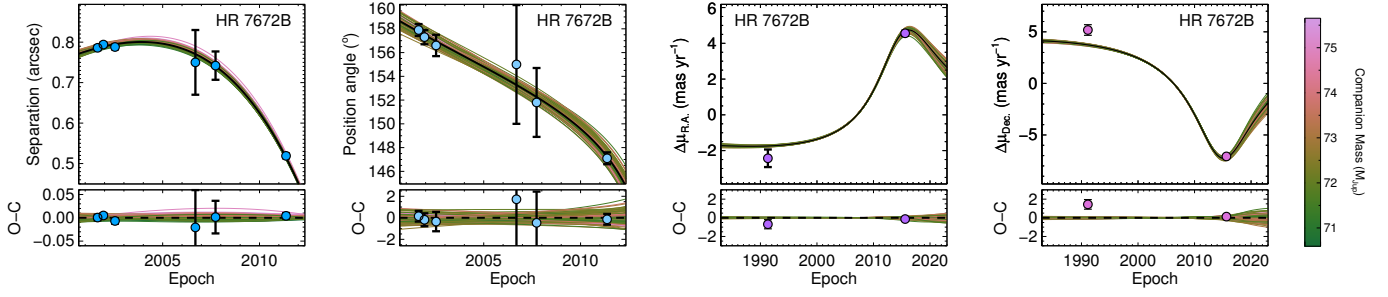


FIG. 24.— Same as Figure 8.

TABLE 6  
MCMC ORBITAL POSTERiors FOR GL 86B AND GL 86 B

Property	Median $\pm 1\sigma$	95.4% c.i.	Prior
Fitted parameters			
Companion mass $M_{\text{comp}}$ ( $M_{\text{Jup}}$ )	$623 \pm 11$	601, 646	$1/M$ (log-flat)
Host-star mass $M_{\text{host}}$ ( $M_{\odot}$ )	$1.36 \pm 0.23$	0.88, 1.83	$1/M$ (log-flat)
Parallax (mas)	$92.70 \pm 0.05$	92.60, 92.80	$\exp[-0.5((\varpi - \varpi_{\text{DR2}})/\sigma[\varpi_{\text{DR2}}])^2]$
Semimajor axis $a$ (AU)	$21.7^{+0.5}_{-0.7}$	20.6, 23.4	$1/a$ (log-flat)
Inclination $i$ ( $^{\circ}$ )	$125.5^{+0.8}_{-0.9}$	123.8, 127.2	$\sin(i)$ , $0^{\circ} < i < 180^{\circ}$
$\sqrt{e} \sin \omega$	$-0.54^{+0.04}_{-0.05}$	-0.62, -0.42	uniform
$\sqrt{e} \cos \omega$	$0.491^{+0.014}_{-0.017}$	0.462, 0.527	uniform
Mean longitude at $t_{\text{ref}} = 2455197.5$ JD, $\lambda_{\text{ref}}$ ( $^{\circ}$ )	$109^{+6}_{-5}$	98, 120	uniform
PA of the ascending node $\Omega$ ( $^{\circ}$ )	$232.4^{+1.7}_{-1.5}$	229.0, 235.4	uniform
Semiamplitude of Gl 86 b ( $\text{m s}^{-1}$ )	$378.9 \pm 1.0$	376.9, 381.1	$1/K_1$ (log-flat)
Orbital period of Gl 86 b $P_{\text{pl}}$ (d)	$15.76486^{+0.00016}_{-0.00017}$	15.76453, 15.76518	$1/P_{\text{pl}}$ (log-flat)
Mean longitude of Gl 86 b at $t_{\text{ref}}$ $\lambda_{\text{ref,plx}}$ ( $^{\circ}$ )	$252.3 \pm 0.6$	251.0, 253.6	uniform
$\sqrt{e_{\text{pl}}} \sin \omega_{\text{pl}}$	$-0.223^{+0.006}_{-0.007}$	-0.235, -0.209	uniform
$\sqrt{e_{\text{pl}}} \cos \omega_{\text{pl}}$	$-0.001 \pm 0.018$	-0.037, 0.036	uniform
RV zero point ( $\text{m s}^{-1}$ )	$230 \pm 40$	160, 310	uniform
RV jitter $\sigma$ ( $\text{m s}^{-1}$ )	$0.00028^{+0.05988}_{-0.00028}$	0.00000, 3.72509	$1/\sigma$ (log-flat)
Computed properties			
Orbital period $P$ (yr)	$72^{+7}_{-8}$	59, 92	...
Semimajor axis (mas)	$2010^{+50}_{-70}$	1910, 2170	...
Eccentricity $e$	$0.53^{+0.04}_{-0.03}$	0.45, 0.60	...
Argument of periastron $\omega$ ( $^{\circ}$ )	$312.5^{+2.8}_{-3.5}$	306.8, 321.1	...
Time of periastron $T_0 = t_{\text{ref}} - P \frac{\lambda - \omega}{360^{\circ}}$ (JD)	$2443700^{+700}_{-600}$	2442300, 2444800	...
Mass ratio $q = M_{\text{comp}}/M_{\text{host}}$	$0.44^{+0.06}_{-0.08}$	0.31, 0.62	...
Eccentricity of Gl 86 b $e_{\text{pl}}$	$0.0498^{+0.0028}_{-0.0029}$	0.0440, 0.0557	...
Argument of periastron of Gl 86 b $\omega_{\text{pl}}$ ( $^{\circ}$ )	$270 \pm 5$	260, 279	...
Time of periastron of Gl 86 b $T_{0,\text{pl}}$ (JD)	$2455198.25^{+0.22}_{-0.21}$	2455197.75, 2455198.75	...

NOTE. — The  $\chi^2$  of relative astrometry is 7.39 for separations and 5.89 for PAs, with 6 measurements for each. The  $\chi^2$  of the Hipparcos and Gaia proper motion differences is 1.39 for four measurements.

TABLE 7  
MCMC ORBITAL POSTERIORI FOR HD 68017B

Property	Median $\pm 1\sigma$	95.4% c.i.	Prior
Fitted parameters			
Companion mass $M_{\text{comp}}$ ( $M_{\text{Jup}}$ )	$154 \pm 3$	148, 161	$1/M$ (log-flat)
Host-star mass $M_{\text{host}}$ ( $M_{\odot}$ )	$0.98 \pm 0.07$	0.83, 1.12	$1/M$ (log-flat)
Parallax (mas)	$46.33 \pm 0.06$	46.21, 46.45	$\exp[-0.5((\varpi - \varpi_{\text{DR2}})/\sigma[\varpi_{\text{DR2}}])^2]$
Semimajor axis $a$ (AU)	$16.0^{+1.0}_{-1.2}$	14.1, 18.5	$1/a$ (log-flat)
Inclination $i$ ( $^{\circ}$ )	$170.3 \pm 0.4$	169.4, 171.1	$\sin(i)$ , $0^{\circ} < i < 180^{\circ}$
$\sqrt{e} \sin \omega$	$-0.56^{+0.03}_{-0.04}$	-0.62, -0.48	uniform
$\sqrt{e} \cos \omega$	$0.10 \pm 0.09$	-0.08, 0.28	uniform
Mean longitude at $t_{\text{ref}} = 2455197.5$ JD, $\lambda_{\text{ref}}$ ( $^{\circ}$ )	$235.1 \pm 0.9$	233.3, 236.9	uniform
PA of the ascending node $\Omega$ ( $^{\circ}$ )	$98.0 \pm 0.9$	96.2, 99.7	uniform
RV zero point ( $\text{m s}^{-1}$ )	$-157^{+14}_{-13}$	-186, -132	uniform
RV jitter $\sigma$ ( $\text{m s}^{-1}$ )	$5.7^{+0.3}_{-0.4}$	5.0, 6.5	$1/\sigma$ (log-flat)
Computed properties			
Orbital period $P$ (yr)	$60^{+6}_{-8}$	48, 78	...
Semimajor axis (mas)	$740^{+40}_{-60}$	650, 860	...
Eccentricity $e$	$0.325^{+0.017}_{-0.024}$	0.292, 0.382	...
Argument of periastron $\omega$ ( $^{\circ}$ )	$280 \pm 10$	262, 300	...
Time of periastron $T_0 = t_{\text{ref}} - P \frac{\lambda - \omega}{360^{\circ}}$ (JD)	$2435900^{+3300}_{-2400}$	2429000, 2440900	...
Mass ratio $q = M_{\text{comp}}/M_{\text{host}}$	$0.150^{+0.010}_{-0.012}$	0.130, 0.174	...

NOTE. — The  $\chi^2$  of relative astrometry is 1.01 for separations and 0.0121 for PAs, with 2 measurements for each. The  $\chi^2$  of the Hipparcos and Gaia proper motion differences is 9.60 for four measurements.

TABLE 8  
MCMC ORBITAL POSTERiors FOR GL 758B

Property	Median $\pm 1\sigma$	95.4% c.i.	Prior
Fitted parameters			
Companion mass $M_{\text{comp}}$ ( $M_{\text{Jup}}$ )	$38.1^{+1.7}_{-1.5}$	35.1, 41.3	$1/M$ (log-flat)
Host-star mass $M_{\text{host}}$ ( $M_{\odot}$ )	$0.76^{+0.13}_{-0.27}$	0.45, 1.21	$1/M$ (log-flat)
Parallax (mas)	$64.061 \pm 0.022$	64.018, 64.106	$\exp[-0.5((\varpi - \varpi_{\text{DR2}})/\sigma[\varpi_{\text{DR2}}])^2]$
Semimajor axis $a$ (AU)	$30^{+5}_{-8}$	21, 46	$1/a$ (log-flat)
Inclination $i$ ( $^{\circ}$ )	$41 \pm 6$	29, 53	$\sin(i)$ , $0^{\circ} < i < 180^{\circ}$
$\sqrt{e} \sin \omega$	$0.27^{+0.35}_{-0.20}$	-0.17, 0.70	uniform
$\sqrt{e} \cos \omega$	$-0.53^{+0.12}_{-0.18}$	-0.74, -0.14	uniform
Mean longitude at $t_{\text{ref}} = 2455197.5$ JD, $\lambda_{\text{ref}}$ ( $^{\circ}$ )	$73^{+14}_{-16}$	42, 101	uniform
PA of the ascending node $\Omega$ ( $^{\circ}$ )	$175^{+6}_{-4}$	161, 184	uniform
McDonald RV zero point ( $\text{m s}^{-1}$ )	$85^{+26}_{-27}$	34, 135	uniform
McDonald RV jitter $\sigma$ ( $\text{m s}^{-1}$ )	$2.9^{+1.1}_{-0.8}$	0.0, 4.2	$1/\sigma$ (log-flat)
Keck RV zero point ( $\text{m s}^{-1}$ )	$74^{+25}_{-28}$	24, 125	uniform
Keck RV jitter $\sigma$ ( $\text{m s}^{-1}$ )	$2.35^{+0.16}_{-0.18}$	2.00, 2.71	$1/\sigma$ (log-flat)
APF RV zero point ( $\text{m s}^{-1}$ )	$67^{+26}_{-27}$	16, 117	uniform
APF RV jitter $\sigma$ ( $\text{m s}^{-1}$ )	$2.50^{+0.17}_{-0.19}$	2.15, 2.87	$1/\sigma$ (log-flat)
Computed properties			
Orbital period $P$ (yr)	$180^{+60}_{-90}$	80, 420	...
Semimajor axis (mas)	$1910^{+300}_{-510}$	1330, 2980	...
Eccentricity $e$	$0.40 \pm 0.09$	0.22, 0.59	...
Argument of periastron $\omega$ ( $^{\circ}$ )	$150 \pm 30$	100, 200	...
Time of periastron $T_0 = t_{\text{ref}} - P \frac{\lambda - \omega}{360^{\circ}}$ (JD)	$2468700^{+1300}_{-1100}$	2465800, 2472000	...
Mass ratio $q = M_{\text{comp}}/M_{\text{host}}$	$0.048^{+0.011}_{-0.015}$	0.026, 0.077	...

NOTE. — The  $\chi^2$  of relative astrometry is 2.70 for separations and 3.94 for PAs, with 4 measurements for each. The  $\chi^2$  of the Hipparcos and Gaia proper motion differences is 3.95 for four measurements.

TABLE 9  
MCMC ORBITAL POSTERiors FOR HR 7672B

Property	Median $\pm 1\sigma$	95.4% c.i.	Prior
Fitted parameters			
Companion mass $M_{\text{comp}}$ ( $M_{\text{Jup}}$ )	$72.7 \pm 0.8$	71.0, 74.3	$1/M$ (log-flat)
Host-star mass $M_{\text{host}}$ ( $M_{\odot}$ )	$0.96^{+0.04}_{-0.05}$	0.87, 1.05	$1/M$ (log-flat)
Parallax (mas)	$56.43 \pm 0.07$	56.29, 56.57	$\exp[-0.5((\varpi - \varpi_{\text{DR2}})/\sigma[\varpi_{\text{DR2}}])^2]$
Semimajor axis $a$ (AU)	$19.6^{+0.8}_{-1.0}$	17.9, 21.7	$1/a$ (log-flat)
Inclination $i$ ( $^{\circ}$ )	$97.4 \pm 0.4$	96.6, 98.3	$\sin(i)$ , $0^{\circ} < i < 180^{\circ}$
$\sqrt{e} \sin \omega$	$-0.715^{+0.006}_{-0.005}$	-0.726, -0.704	uniform
$\sqrt{e} \cos \omega$	$-0.17 \pm 0.04$	-0.25, -0.10	uniform
Mean longitude at $t_{\text{ref}} = 2455197.5$ JD, $\lambda_{\text{ref}}$ ( $^{\circ}$ )	$237.1^{+0.6}_{-0.7}$	235.8, 238.4	uniform
PA of the ascending node $\Omega$ ( $^{\circ}$ )	$330.95^{+0.32}_{-0.30}$	330.32, 331.56	uniform
RV zero point ( $\text{m s}^{-1}$ )	$-602 \pm 19$	-642, -565	uniform
RV jitter $\sigma$ ( $\text{m s}^{-1}$ )	$5.8 \pm 0.3$	5.2, 6.5	$1/\sigma$ (log-flat)
Computed properties			
Orbital period $P$ (yr)	$86^{+7}_{-8}$	72, 102	...
Semimajor axis (mas)	$1110^{+50}_{-60}$	1010, 1220	...
Eccentricity $e$	$0.542 \pm 0.018$	0.507, 0.581	...
Argument of periastron $\omega$ ( $^{\circ}$ )	$256.3^{+2.8}_{-2.7}$	250.9, 261.9	...
Time of periastron $T_0 = t_{\text{ref}} - P \frac{\lambda - \omega}{360^{\circ}}$ (JD)	$2425600^{+2900}_{-2600}$	2419400, 2430700	...
Mass ratio $q = M_{\text{comp}}/M_{\text{host}}$	$0.0722 \pm 0.0030$	0.0664, 0.0784	...

NOTE. — The  $\chi^2$  of relative astrometry is 2.83 for separations and 0.553 for PAs, with 6 measurements for each. The  $\chi^2$  of the Hipparcos and Gaia proper motion differences is 11.4 for four measurements.

## REFERENCES

- Baliunas, S. L., Donahue, R. A., Soon, W. H., et al. 1995, *ApJ*, 438, 269
- Baraffe, I., Chabrier, G., Barman, T. S., Allard, F., & Hauschildt, P. H. 2003, *A&A*, 402, 701
- Barnes, S. A. 2003, *ApJ*, 586, 464
- Benedict, G. F., McArthur, B. E., Forveille, T., et al. 2002, *ApJ*, 581, L115
- Beuzit, J.-L., Demailly, L., Gendron, E., et al. 1997, *Experimental Astronomy*, 7, 285
- Boccaletti, A., Chauvin, G., Lagrange, A.-M., & Marchis, F. 2003, *A&A*, 410, 283
- Bond, H. E., Bergeron, P., & Bédard, A. 2017, *ApJ*, 848, 16
- Bowler, B. P., Dupuy, T. J., Endl, M., et al. 2018, *AJ*, 155, 159
- Bowler, B. P., Liu, M. C., Shkolnik, E. L., & Tamura, M. 2015, *ApJS*, 216, 7
- Brandt, T. D. 2018, submitted
- Brandt, T. D., Kuzuhara, M., McElwain, M. W., et al. 2014, *ApJ*, 786, 1
- Bressan, A., Marigo, P., Girardi, L., et al. 2012, *MNRAS*, 427, 127
- Brewer, J. M., Fischer, D. A., Valenti, J. A., & Piskunov, N. 2016, *The Astrophysical Journal Supplement Series*, 225
- Burrows, A., Marley, M., Hubbard, W. B., et al. 1997, *ApJ*, 491, 856
- Butler, R. P., Vogt, S. S., Laughlin, G., et al. 2017, *AJ*, 153, 208
- Butler, R. P., Wright, J. T., Marcy, G. W., et al. 2006, *ApJ*, 646, 505
- Calissendorff, P., & Janson, M. 2018, *ArXiv e-prints*, 1806.07899
- Cheetham, A., Ségransan, D., Peretti, S., et al. 2018, *A&A*, 614, A16
- Cochran, W. D., Hatzes, A. P., Butler, R. P., & Marcy, G. W. 1997, *ApJ*, 483, 457
- Crepp, J. R., Gonzales, E. J., Bechter, E. B., et al. 2016, *ApJ*, 831, 136
- Crepp, J. R., Johnson, J. A., Fischer, D. A., et al. 2012a, *ApJ*, 751, 97
- Crepp, J. R., Johnson, J. A., Howard, A. W., et al. 2012b, *ApJ*, 761, 39
- Crepp, J. R., Principe, D. A., Wolff, S., et al. 2018, *ApJ*, 853, 192
- Crepp, J. R., Rice, E. L., Veicht, A., et al. 2015, *ApJ*, 798, L43
- Cumming, A., Marcy, G. W., & Butler, R. P. 1999, *ApJ*, 526, 890
- Cutri, R. M., Skrutskie, M. F., van Dyk, S., et al. 2003, *VizieR Online Data Catalog*, 2246
- Delfosse, X., Forveille, T., Ségransan, D., et al. 2000, *A&A*, 364, 217
- Demarque, P., Woo, J.-H., Kim, Y.-C., & Yi, S. K. 2004, *ApJS*, 155, 667
- Diego, F., Charalambous, A., Fish, A. C., & Walker, D. D. 1990, in *SPIE*, Vol. 1235, *Instrumentation in Astronomy VII*, ed. D. L. Crawford, 562
- Dieterich, S. B., Weinberger, A. J., Boss, A. P., et al. 2018, *ArXiv e-prints*, arXiv:1807.09880
- Dotter, A., Chaboyer, B., Jevremović, D., et al. 2008, *The Astrophysical Journal Supplement Series*, 178, 89
- Ducati, J. R. 2002, *VizieR Online Data Catalog*
- Dupuy, T. J., & Liu, M. C. 2017, *ApJS*, 231, 15
- Dupuy, T. J., Liu, M. C., & Ireland, M. J. 2009a, *ApJ*, 692, 729
- Dupuy, T. J., Liu, M. C., & Ireland, M. J. 2009b, *ApJ*, 699, 168
- Earl, D. J., & Deem, M. W. 2005, *Physical Chemistry Chemical Physics (Incorporating Faraday Transactions)*, 7, 3910
- Els, S. G., Sterzik, M. F., Marchis, F., et al. 2001, *A&A*, 370, L1
- Endl, M., Brugamyer, E. J., Cochran, W. D., et al. 2016, *ApJ*, 818, 34
- ESA, ed. 1997, *ESA Special Publication*, Vol. 1200, *The HIPPARCOS and TYCHO catalogues. Astrometric and photometric star catalogues derived from the ESA HIPPARCOS Space Astrometry Mission*
- Farihi, J., Bond, H. E., Dufour, P., et al. 2013, *MNRAS*, 430, 652
- Fey, A. L., Gordon, D., Jacobs, C. S., et al. 2015, *AJ*, 150, 58
- Filippazzo, J. C., Rice, E. L., Faherty, J., et al. 2015, *ApJ*, 810, 158
- Fontaine, G., Brassard, P., & Bergeron, P. 2001, *PASP*, 113, 409
- Foreman-Mackey, D., Hogg, D. W., Lang, D., & Goodman, J. 2013, *PASP*, 125, 306
- Fortney, J. J., Marley, M. S., Saumon, D., & Lodders, K. 2008, *ApJ*, 683, 1104
- Fuhrmann, K. 2004, *Astronomische Nachrichten*, 325, 3
- Fuhrmann, K., Chini, R., Buda, L.-S., & Pozo Nuñez, F. 2014, *ApJ*, 785, 68
- Fulton, B. J., Weiss, L. M., Sinukoff, E., et al. 2015, *ApJ*, 805, 175
- Gaia Collaboration, Brown, A. G. A., Vallenari, A., et al. 2018, *A&A*, 616, A1
- Gaia Collaboration, Prusti, T., de Bruijne, J. H. J., et al. 2016, *A&A*, 595, A1
- Graves, J. E., Northcott, M. J., Roddier, F. J., Roddier, C. A., & Close, L. M. 1998, in *SPIE*, Vol. 3353, *Adaptive Optical System Technologies*, ed. D. Bonaccini & R. K. Tyson, 34
- Gray, R. O., Corbally, C. J., Garrison, R. F., et al. 2006, *AJ*, 132, 161
- Gray, R. O., Corbally, C. J., Garrison, R. F., McFadden, M. T., & Robinson, P. E. 2003, *AJ*, 126, 2048
- Han, I., Black, D. C., & Gatewood, G. 2001, *ApJ*, 548, L57
- Harris, H. C., Dahn, C. C., Dupuy, T. J., et al. 2013, *ApJ*, 779, 21
- Hillenbrand, L. A., & White, R. J. 2004, *ApJ*, 604, 741
- Høg, E., Fabricius, C., Makarov, V. V., et al. 2000, *A&A*, 355, L27
- Houk, N., & Smith-Moore, M. 1988, *Michigan Catalogue of Two-dimensional Spectral Types for the HD Stars. Volume 4, Declinations -26°.0 to -12°.0*
- Howard, A. W., Johnson, J. A., Marcy, G. W., et al. 2010, *ApJ*, 721, 1467
- Janson, M., Carson, J., Thalmann, C., et al. 2011, *ApJ*, 728, 85
- King, R. R., McCaughrean, M. J., Homeier, D., et al. 2010, *A&A*, 510, A99
- Konopacky, Q. M., Ghez, A. M., Barman, T. S., et al. 2010, *ApJ*, 711, 1087
- Lafrenière, D., Marois, C., Doyon, R., Nadeau, D., & Artigau, É. 2007, *ApJ*, 660, 770
- Lagrange, A.-M., Beust, H., Udry, S., Chauvin, G., & Mayor, M. 2006, *A&A*, 459, 955
- Lenzen, R., Hartung, M., Brandner, W., et al. 2003, in *SPIE*, Vol. 4841, *Instrument Design and Performance for Optical/Infrared Ground-based Telescopes*, ed. M. Iye & A. F. M. Moorwood, 944
- Lindgren, L., Hernandez, J., Bombrun, A., et al. 2018, *arxiv*, 1804.09366
- Liu, M. C., Fischer, D. A., Graham, J. R., et al. 2002, *ApJ*, 571, 519
- Ma, C., Arias, E. F., Eubanks, T. M., et al. 1998, *AJ*, 116, 516
- Mamajek, E. E., & Hillenbrand, L. A. 2008, *ApJ*, 687, 1264
- Marleau, G.-D., & Cumming, A. 2014, *MNRAS*, 437, 1378
- Marley, M. S., Fortney, J. J., Hubickyj, O., Bodenheimer, P., & Lissauer, J. J. 2007, *ApJ*, 655, 541
- Marois, C., Lafrenière, D., Doyon, R., Macintosh, B., & Nadeau, D. 2006, *ApJ*, 641, 556
- Mestel, L. 1968, *MNRAS*, 138, 359
- Mishenina, T. V., Soubiran, C., Kovtyukh, V. V., & Korotin, S. A. 2004, *A&A*, 418, 551
- Montet, B. T., Bowler, B. P., Shkolnik, E. L., et al. 2015, *ApJ*, 813, L11
- Mugrauer, M., & Neuhäuser, R. 2005, *MNRAS*, 361, L15
- Noyes, R. W., Hartmann, L. W., Baliunas, S. L., Duncan, D. K., & Vaughan, A. H. 1984, *ApJ*, 279, 763
- Pace, G. 2013, *A&A*, 551, L8
- Peretti, S., Ségransan, D., Lavie, B., et al. 2018, *ArXiv e-prints*, 1805.05645
- Plewa, P. M., Gillessen, S., Eisenhauer, F., et al. 2015, *MNRAS*, 453, 3234
- Pourbaix, D., & Arenou, F. 2001, *A&A*, 372, 935
- Queloz, D., Mayor, M., Weber, L., et al. 2000, *A&A*, 354, 99
- Ramírez, I., Allende Prieto, C., & Lambert, D. L. 2007, *A&A*, 465, 271
- Ramírez, I., Allende Prieto, C., & Lambert, D. L. 2013, *ApJ*, 764, 78
- Rocha-Pinto, H. J., Castilho, B. V., & Maciel, W. J. 2002, *A&A*, 384, 912
- Rousset, G., Lacombe, F., Puget, P., et al. 2003, in *SPIE*, Vol. 4839, *Adaptive Optical System Technologies II*, ed. P. L. Wizinowich & D. Bonaccini, 140
- Sahlmann, J., Ségransan, D., Queloz, D., et al. 2011, *A&A*, 525, A95
- Salpeter, E. E. 1955, *ApJ*, 121, 161
- Saumon, D., & Marley, M. S. 2008, *ApJ*, 689, 1327
- Saumon, D., & Marley, M. S. 2008, *ApJ*, 689, 1327
- Serabyn, E., Mawet, D., Bloemhof, E., et al. 2009, *ApJ*, 696, 40
- Service, M., Lu, J. R., Campbell, R., et al. 2016, *PASP*, 128, 095004
- Snellen, I. A. G., & Brown, A. G. A. 2018, *Nature Astronomy*, 1808.06257
- Soderblom, D. R. 2010, *ARA&A*, 48, 581
- Soubiran, C., Le Campion, J.-F., Brouillet, N., & Chemin, L. 2016, *A&A*, 591, A118
- Sozzetti, A., & Desidera, S. 2010, *A&A*, 509, A103
- Spada, F., Demarque, P., Kim, Y.-C., & Sills, A. 2013, *ApJ*, 776, 87
- Spiegel, D. S., & Burrows, A. 2012, *ApJ*, 745, 174
- Stassun, K. G., Mathieu, R. D., & Valenti, J. A. 2006, *Natur*, 440, 311
- Takeda, Y., Kawanomoto, S., Honda, S., Ando, H., & Sakurai, T. 2007, *A&A*, 468, 663



- Thalmann, C., Carson, J., Janson, M., et al. 2009, *ApJ*, 707, L123
- Troy, M., Dekany, R. G., Brack, G., et al. 2000, in *SPIE*, Vol. 4007, *Adaptive Optical Systems Technology*, ed. P. L. Wizinowich, 31
- Tull, R. G., MacQueen, P. J., Sneden, C., & Lambert, D. L. 1995, *PASP*, 107, 251
- Valenti, J. A., & Fischer, D. A. 2005, *The Astrophysical Journal Supplement Series*, 159, 141
- van Leeuwen, F. 2007, *A&A*, 474, 653
- van Saders, J. L., Ceillier, T., Metcalfe, T. S., et al. 2016, *Natur*, 529, 181
- Vigan, A., Bonnefoy, M., Ginski, C., et al. 2016, *A&A*, 587, A55
- Voges, W., Aschenbach, B., Boller, T., et al. 1999, *A&A*, 349, 389
- Vogt, S. S., Allen, S. L., Bigelow, B. C., et al. 1994, in *SPIE*, Vol. 2198, *Instrumentation in Astronomy VIII*, ed. D. L. Crawford & E. R. Craine, 362
- Vogt, S. S., Radovan, M., Kibrick, R., et al. 2014, *PASP*, 126, 359
- Wizinowich, P., Acton, D. S., Shelton, C., et al. 2000, *PASP*, 112, 315
- Wright, N. J., Drake, J. J., Mamajek, E. E., & Henry, G. W. 2011, *ApJ*, 743, 48
- Yelda, S., Lu, J. R., Ghez, A. M., et al. 2010, *ApJ*, 725, 331